**DOKUZ EYLÜL UNIVERSITY**

**GRADUATE SCHOOL OF NATURAL AND APPLIED SCIENCES**

# PRODUCTION OF PIEZOELECTRIC BIOMATERIALS FOR TISSUE ENGINEERING APPLICATIONS

**by**

**Neslihan ŞAKAR**

**July, 2024**

**İZMİR**

# PRODUCTION OF PIEZOELECTRIC BIOMATERIALS FOR TISSUE ENGINEERING APPLICATIONS

**A Thesis Submitted to the**
**Graduate School of Natural and Applied Sciences of Dokuz Eylül University**
**In Partial Fulfillment of the Requirements for the Degree of Doctor of Philosophy in Department of Nanoscience and Nanoengineering, Nanoscience and Nanoengineering Program**

**By**

**Neslihan ŞAKAR**

**July, 2024**

**İZMİR**

**Ph.D. THESIS EXAMINATION RESULT FORM**

We have read the thesis entitled **"PRODUCTION OF PIEZOELECTRIC BIOMATERIALS FOR TISSUE ENGINEERING APPLICATIONS "** completed by **NESLİHAN SAKAR** under supervision of **ASSOC.PROF.DR. AYLIN ZIYLAN** and we certify that in our opinion it is fully adequate, in scope and in quality, as a thesis for the degree of Doctor of Philosophy.

Assoc.Prof.Dr. Aylin ZIYLAN

Supervisor

| | |
|---|---|
| Prof.Dr. Mucahit SUTCU | Assoc.Prof.Dr. Mustafa EROL |
| Thesis Committee Member | Thesis Committee Member |
| Assoc.Prof.Dr. Umut Adem | Assoc.Prof.Dr. Tunay Tansel |
| Examining Committee Member | Examining Committee Member |

Prof. Dr. Okan FISTIKOĞLU

Director

Graduate School of Natural and Applied Sciences

## ACKNOWLEDGMENT

First of all, I would like to thank my esteemed advisor, Assoc. Prof. Dr. Aylin Ziylan, for always believing, encouraging, and supporting me. I will always be proud to be her student.

I want to thank my esteemed thesis jury members Prof. Dr. Mücahit Sütçü and Assoc. Prof. Dr. Mustafa Erol guided me the right way throughout the process. Also, I would like to thank Assoc. Prof. Dr. Umut Adem, Assoc. Prof. Dr. Tunay Tansel and Dr. Merve Karakaya for supporting and encouraging the thesis study.

This study is financially supported by TUBITAK - Short-Term R&D Funding Program (Project Number 222M340). The authors are indebted to the infrastructural support from Dokuz Eylul University, the Center for Production and Applications of Electronic Materials (EMUM) where the research was carried out. Also, Neslihan Sakar is supported by the Turkish Higher Education Council's 100/2000 Ph.D. Fellowship and TUBITAK 2211-C National PhD Scholarship Program. I appreciate their support and thank them.

I would also like to thank my dear friend MSc. Sevcan Kardelen, Assoc. Prof. Dr. Sibel Oğuzlar, Dr. Hilmiye Deniz Ertuğrul Uygun, MSc. Begüm Uzunbayır, Dr. Oylum Çolpankan, and Dr. Gizem Türkoğlu for not leaving me alone during my difficult times. I would like to thank my dear husband Assoc. Prof. Dr. Gökhan Şakar, my father Halil Birinci, my brother Serhat Birinci, my mother Güler Birinci, and my sister Prof. Dr. Ayşın Şakar, who believed in my success from the very beginning and always supported and helped me. Finally, my dear children Uras and Barlas, thank you so much for your endless love and patience.

Neslihan ŞAKAR

**PRODUCTION OF PIEZOELECTRIC BIOMATERIALS FOR TISSUE ENGINEERING APPLICATIONS**

## ABSTRACT

Designing a novel injectable bone cement is crucial for successful bone healing in minimally invasive surgeries. Since natural bone has piezoelectric properties that are essential for bone regeneration, this study is focused on the development of a novel injectable composite bone cement with piezoelectric properties. The composite composition incorporates calcium and zirconium doped barium titanate (BCZT) for its piezoelectric property, alongside the use of calcium phosphate and magnesium phosphate cement (CMPC) for its bone-like properties. In this framework, the first step involved the preparation of BCZT, CMPC, and their composites, followed by an investigation of their phase structures, morphologic structure, particle size distributions, and piezoelectric and dielectric properties. The process involved in preparing the composite bone cements included the mixing of CMPC with BCZT in three different ratios (20, 30, and 40 weight percentage). Following this, a polysorbate 80 solution was added to the cement mixtures to create injectable pastes. Subsequently, the injectability, setting time, and compressive strength of the composites were thoroughly evaluated. The findings indicated that the composite bone cement containing 30 percentage BCZT exhibited notable potential for utilization as an injectable bone cement in invasive orthopedic surgery.

**Keywords:** Bone cement, bone regeneration, injectable, piezoelectric, corona poling

# DOKU MÜHENDİSLİĞİ UYGULAMALARI İÇİN PİEZOELEKTRİK BİYOMALZEMELERİN ÜRETİMİ

## ÖZ

Yeni bir enjekte edilebilir kemik çimentosu tasarlanması, minimal invaziv ameliyatlarda başarılı kemik iyileşmesi için çok önemlidir. Doğal kemik, kemik rejenerasyonu için gerekli olan piezoelektrik özelliklere sahip olduğundan, bu çalışma piezoelektrik özelliklere sahip yeni bir enjekte edilebilir kompozit kemik çimentosunun geliştirilmesine odaklanmıştır. Kompozit bileşim, piezoelektrik özelliği için kalsiyum ve zirkonyum katkılı baryum titanat (BCZT) ve kemik benzeri özellikleri için kalsiyum fosfat ve magnezyum fosfat çimento (CMPC) kullanımını içermektedir. Bu çerçevede, ilk adım BCZT, CMPC ve bunların kompozitlerinin hazırlanması ve ardından faz ve morfolojik yapılarının, partikül boyutu dağılımlarının ve piezoelektrik ve dielektrik özelliklerinin incelenmesini içermektedir. Kompozit kemik çimentolarının hazırlanmasındaki süreç, CMPC'nin BCZT ile üç farklı oranda (ağırlıkça yüzde 20, yüzde 30 ve yüzde 40) karıştırılmasını içermektedir. Bunu takiben, enjekte edilebilir macunlar oluşturmak için çimento karışımlarına bir polisorbat 80 çözeltisi eklenmiştir. Daha sonra, kompozitlerin enjekte edilebilirliği, katılaşma süresi ve basma dayanımı kapsamlı bir şekilde değerlendirilmiştir. Bulgular, yüzde 30 BCZT içeren kompozit kemik çimentosunun invaziv ortopedik cerrahide enjekte edilebilir kemik çimentosu olarak kullanımının kayda değer bir potansiyel sergilediğini göstermiştir.

**Anahtar kelimeler:** Kemik çimentosu, kemik rejenerasyonu, enjekte edilebilir, piezoelektrik, korona kutuplama

**CONTENTS**

**Page**

## LIST OF FIGURES

**Page**

## LIST OF TABLES

**Page**

## LIST OF SYMBOLS

| | |
|---|---|
| $d_{33}$ | : Piezoelectric coefficient |
| °C | : Centigrade (Degree Celsius) |
| Ɛr | : Dielectric constant |
| MPa | : Mega pascal |
| Ca | : Calcium |
| Mg | : Magnesium |
| P | : Phosphate |
| O | : Oxygen |
| Ba | : Barium |
| Ti | : Titanium |

**ABBREVIATIONS**

| | |
|---|---|
| $Sr^{2+}$ | : Strontium ion |
| $Ca^{2+}$ | : Calcium ion |
| $Zr^{4+}$ | : Zirconium ion |
| BCZT | : Barium calcium zirconium titanate |
| CPC | : Calcium phosphate cement |
| MPC | : Magnesium phosphate cement |
| CMPC | : Calcium-magnesium phosphate cement |
| XRD | : X-ray diffraction |
| SEM | : Scanning electron microscopy |
| EDS | : Energy Dispersive X-ray Spectrometer |
| ECM | : Extracellular matrix |
| P/L | : Powder-to-liquid ratio |
| *ti* | *:* Initial setting time |
| *tf* | : Final setting time |
| TTCP | : Tetracalcium phosphate |
| DCPA | : Dicalcium phosphate anhydrous |
| PVA | : Polyvinyl alcohol |
| DCPD | : Dicalcium phosphate dihydrate |

# CHAPTER ONE
# INTRODUCTION

Tissue engineering draws on engineering, chemistry, physics, and biology. Many studies are being conducted to heal damaged tissues such as skin, cartilage, and bone. Engaging in research motivates the advancement of existing biomaterials or the innovation of novel biomaterials. The number of patients who need medical support due to bone tissue damage is increasing day by day. The capacity to mimic natural bone effectively plays a vital role in this field. The production of tissue scaffolds using materials with similar components to bone and can mimic it is of great importance for this field. Natural bone is a composite material composed mostly of calcium and phosphate minerals and is known to have piezoelectric properties. Piezoelectric biomaterials have recently been of great interest for tissue engineering applications. This is since these materials can enhance tissue regeneration when pressure is exerted.

This thesis focuses on the design of a tissue scaffold for the healing of bone damage. The designed scaffold aims to impart piezoelectric properties to bone-like phosphate-based bone cement. An injectable composite was prepared for this purpose. Various studies were conducted to determine the properties of the produced injectable piezoelectric bone cement.

This thesis consists of five main chapters. Chapter one provides information about the main objective and topic of the thesis, while chapter two contains the theoretical background. Chapter three provides a detailed account of the materials and methods utilized in the study, delving into the intricacies of the production and characterization processes for each component. Moving forward, Chapter four expounds upon the results, offering a comprehensive discussion that sheds light on their implications. Finally, Chapter five encapsulates the study with a thorough examination of the conclusions drawn, providing valuable insights and potential avenues for further exploration.

## 1.1 Purpose & Scope

The number of patients with bone damage is increasing day by day due to the aging of the population, and environmental and genetic factors. For this reason, orthopedic surgeries due to bone tissue damage are one of the most common operations. The natural self-healing capacity of bone tissue allows it to continue functioning for a lifetime. Age, genetics, environment, and socioeconomic factors all affect how quickly bones recover. Tissue scaffolds can promote bone tissue regeneration in the injured area and biodegrade after healing in situations when bone healing is compromised. Numerous studies have concentrated on designing bone scaffolds utilizing different biomaterials and/or tissue engineering techniques to mend broken bone (F. Chen et al., 2015; Kapat et al., 2020; Kim & Jeon, 2012; Montufar et al., 2013; Şahin & Kalyon, 2017; Tavangar et al., 2020). The goal of a bone scaffold is to replicate the form and functionality of a real bone, which is made up of collagen fibers reinforced by the mineral hydroxyapatite. This natural composite also possesses piezoelectric qualities (Fukada & Yasuda, 1957). Human bone's piezoelectric coefficient, or $d_{33}$, was 0.7 pC/N (Bur, 1976).

Bone exhibits a piezoelectric property, meaning surface charges are created when stressed. The generation of these charges stimulates bone-building osteoblast cells and thus accelerates healing. (Khare et al., 2020; Tariverdian et al., 2019; Yu et al., 2011). Hence, it can be concluded that the usage of piezoelectric biomaterials in scaffolds facilitates faster bone regeneration by imitating the properties of natural bone (Kapat et al., 2020; Khare et al., 2020; Tavangar et al., 2020). Barium titanate is commonly utilized as a piezoelectric biomaterial (Vouilloz et al., 2017; X. Zhang et al., 2016; Y. Zhang et al., 2014), and its piezoelectric coefficient can be increased by ion doping such as $Sr^{2+}$, $Ca^{2+}$, and $Zr^{4+}$. In this context, the material barium calcium zirconium titanate (BCZT), which is Ca and Zr doped $BaTiO_3$, has gained significant attention as it is both non-toxic and biocompatible, making it a standout among other piezoelectric materials (Manohar et al., 2019; Tariverdian et al., 2019).

Additionally, because of their similar mineral structure, bone cement is an excellent tool for mimicking natural bone. It is especially useful in the treatment of complex

bone damage. Without requiring open surgery, it can be injected directly into the damaged area using minimally invasive surgery. Moreover, it is easily adapted to areas of bone damage and hardens in vivo at the injection site. Bone cement also has special qualities like biocompatibility and biodegradability in addition to these benefits.(F. Chen et al., 2015; Kim & Jeon, 2012; Şahin & Kalyon, 2017; D. Wang et al., 2014). Among these, calcium phosphate cement (CPC) and magnesium phosphate cement (MPC) are crucial for bone repair and regeneration.

In this study, we aim to innovate by designing a novel injectable composite bone cement that contains BCZT-added CMPC with piezoelectric properties. This marks the first instance that CPC, MPC, and BCZT have been combined to create an injectable bone cement that can be used to treat defects in the bones. As the flow of the study, first CPC, MPC, and BCZT powders were produced in that order. Then, their phase and morphologic structures, particle size distributions, dielectric constants, and piezoelectric coefficients were examined by X-ray diffraction (XRD), particle size analyzer, LCR meter, and $d_{33}$ meter, respectively. Finally, the injectability, setting time, and consequent compressive strengths of the piezoelectric composite cement were assessed in light of their possible uses in orthopedic surgery.

# CHAPTER TWO
# THEORITICAL BACKGROUND

## 2.1 Bone Tissue Engineering

Tissue engineering can be defined as an interdisciplinary field a latterly developing field of a combination of biology, material science and engineering, and nanoscience and nanoengineering to develop functional substitutes for damaged tissues. According to the wide range of applications on cell types, it can be divided into skin, bone, vascular, kidney, and liver tissue engineering. After years of powerful progress, a set of novel tissue culture, replacement, and implantation technologies have been developed, allowing fabricating artificial extracellular matrices, called scaffolds, to bear stem cells, growth factors, or other biological nutrients aiming at repairing tissue function. Scaffolds are bulk bioactive materials with specific porosity and structure to contribute to the formation of new tissues for completing the medical task (Karabay et al., 2019).

Tissue scaffolds are designed as structures on which cells can grow and acquire tissue properties and are generally produced using biocompatible and biodegradable ceramic, metal, polymer, or composite biomaterials. The tissue scaffold should have the same structure and biological function as the natural extracellular matrix (ECM) in terms of both chemical composition and physical structure. Biomaterials used; should maintain their structural integrity during the healing process, their mechanical strength should be suitable for the target area, they should show degradation in proportion to the speed with which the target tissue heals, and should be porous enough to allow the tissue to develop within the structure, and they should be able to imitate the natural three-dimensional structure of the tissue (Thomas et al., 2016).

Many studies continue from past to present to produce an ideal bone tissue scaffold that can have all the features above at the same time. These studies mostly focused on developing new materials and new production methods. However, the success of these developments depends on how well the natural bone structure can be imitated. As seen in Figure 2.1, natural bone; is an electrically active composite (polymer-ceramic)

material consisting of different components such as inorganic (hydroxyapatite), organic (collagen), cellular (osteoblast, osteoclast, osteocytes), and water (Dubey & Kakimoto, 2016; Lang, 2016; Vouilloz et al., 2017)

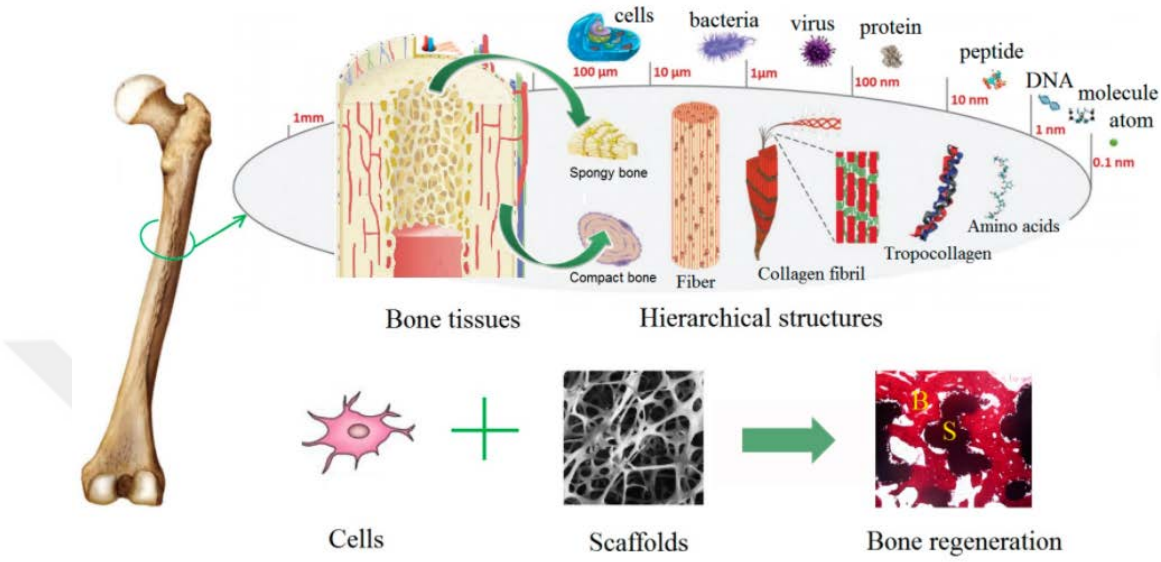


Figure 2.1 The hierarchical anatomy structures of bone tissues. Bone regeneration strategy is conducted by the synergistic effect of cells and scaffolds (X. Chen et al., 2018)

Also, natural bone has piezoelectric properties (Fukada & Yasuda, 1957). Due to the mechanical stress caused by daily activities, positive and negative electrical charges occur in the bone. The piezoelectric property of the bone and the resulting positive and negative charges contribute to the activity of cells that provide bone resorption (osteoclasts) and bone-forming (osteoblasts) (Tavangar et al., 2020)

## 2.2 Biomaterials

Biomaterials contact living tissue and can replace or enhance certain body components to improve or restore function. The diverse properties of biomaterials, including mechanical, biological, physical, and chemical aspects, play a crucial role in their functionality and applicability in the human body (Bhat & Kumar, 2013).

On the other hand, there are some important properties that a material must have to be a biomaterial and these properties are given in Figure 2.2 with their definitions.

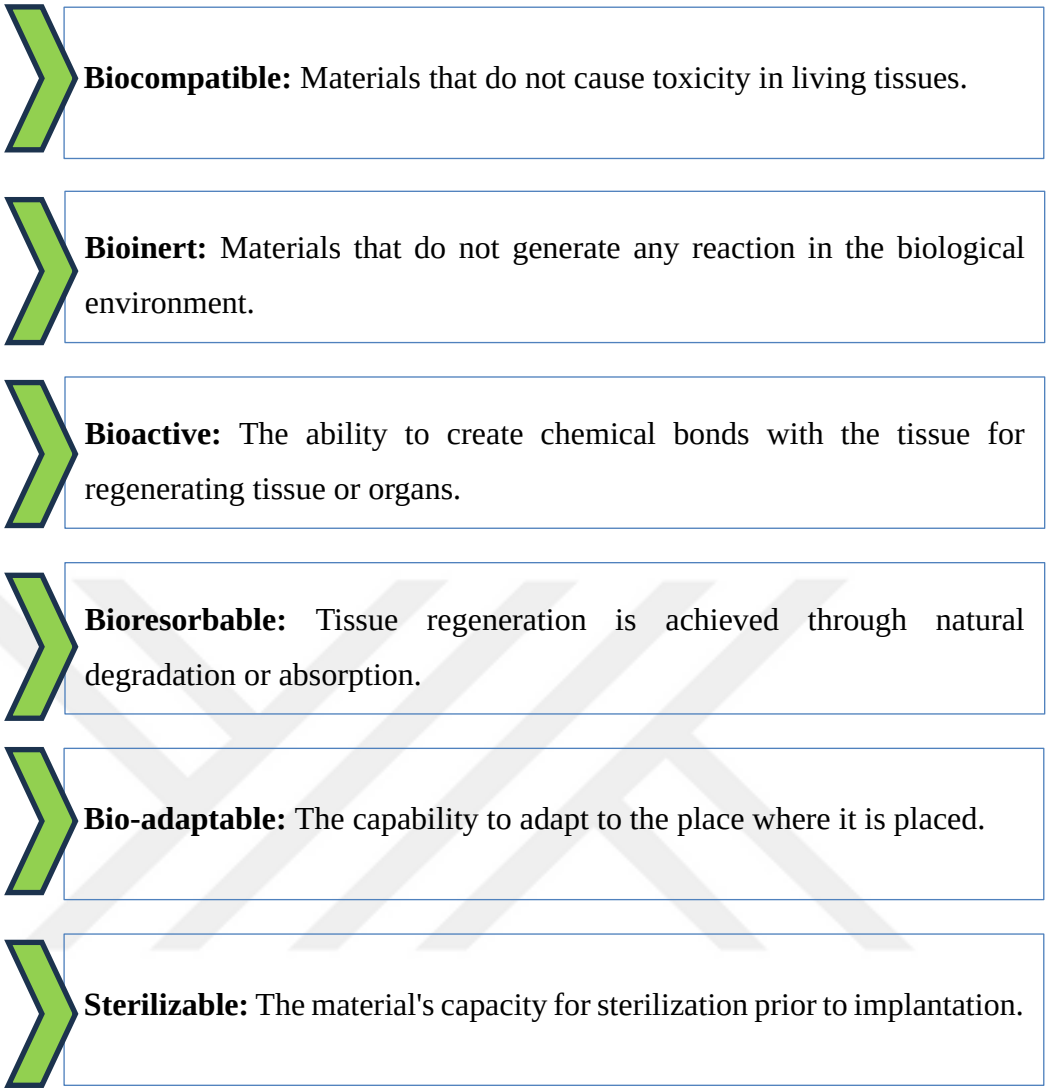


Figure 2.2 The flow chart of the ideal characteristics of a biomaterial (Paul, 2019)

Biomaterials can be classified based on different criteria such as their chemical composition, origin, function, degradation characteristics, and application fields (Arjunan et al., 2020; Bharadwaj, 2021; Jiann Chong et al., 2023; Türk et al., 2023). Herein, the classification of biomaterials based on chemical composition is preferred and given in Figure 2.3. Several important groups of biomaterials are widely used in biomedical applications, including ceramics, polymers, metals, and composites (Kulinets, 2015).

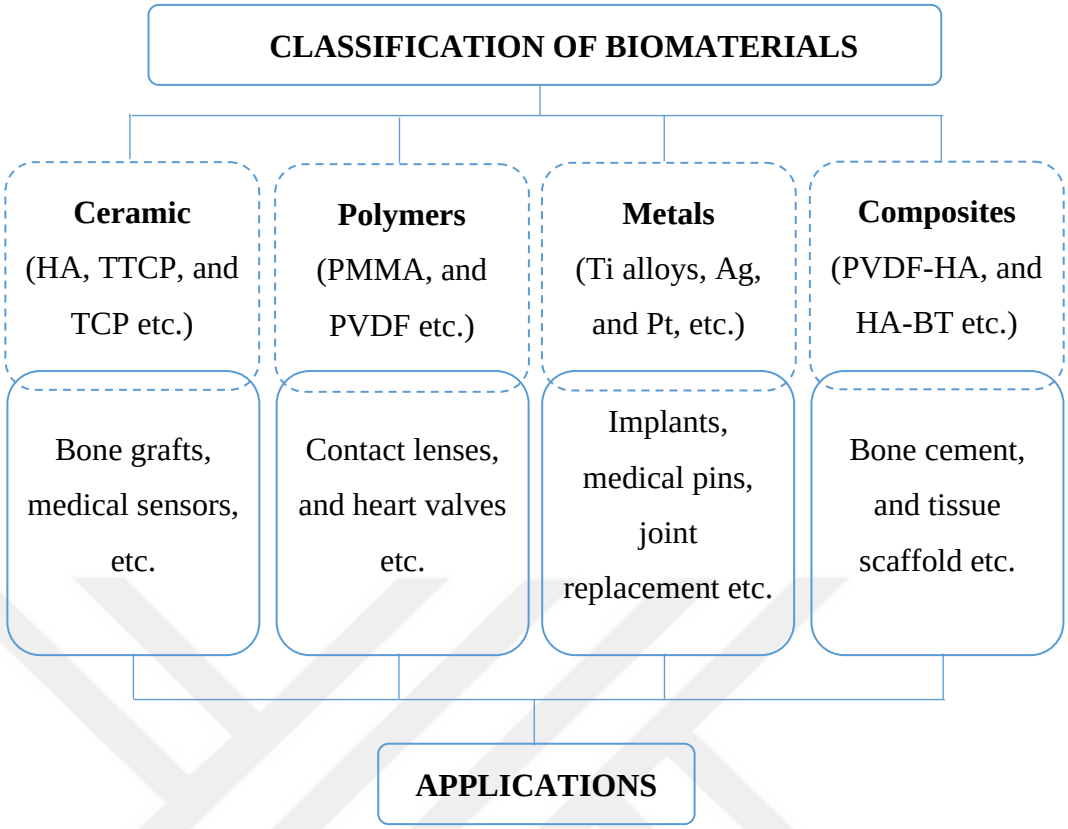


Figure 2.3 Classification of biomaterials based on chemical composition (Bharadwaj, 2021; Kulinets, 2015)

### *2.2.1 Bioceramics*

Bioceramics have unique features that set them apart from other biomaterials like metals or polymers. These features include high intrinsic strength, biocompatibility, and versatility (Vaiani et al., 2023).

Bioceramics have excellent mechanical properties, such as good wear resistance and a low coefficient of friction, exhibited by materials like zirconia and alumina, which are suitable for use in high-stress applications like dental implants or artificial joints. On the other hand, the risk of negative responses or inflammation is often lower with bioceramics because they are compatible with human tissues. Certain bioceramics, including hydroxyapatite or bioactive glasses, exhibit bioactive characteristics that may promote tissue regeneration and osteointegration (Bohner, 2008; Paul, 2019; Vaiani et al., 2023). Another important property of bioceramics is versatility, and because of this property, they can be shaped with precision, and their

compositions can be customized to enhance specific characteristics. Because of all these advantages, bioceramics can be used to solve a wide range of biomedical problems. The field of ceramic biomaterials exhibits remarkable growth, with new and significant applications emerging in medicine and biotechnology (Bharadwaj, 2021). These applications include ceramic biomaterials such as fillers, load-bearing parts, biomimetic scaffolds, drug delivery platforms, veneering materials, and joint replacements (Vaiani et al., 2023).

Ceramics is a significant group of bioceramics divided into three classes which are bioinert, bioactive, and bioresorbable. Ceramics are mostly bioactive materials, including apatite-wollastonite glass ceramic and hydroxyapatite.

### *2.2.2 Biopolymers*

The polymers occur from repeating units which are called monomers. Polymers that have biomaterial properties are called biopolymers. The various uses of polymeric biomaterials in tissue engineering and biomedical fields are depicted in Figure 2.4 (Kalirajan et al., 2021; Paul, 2019).

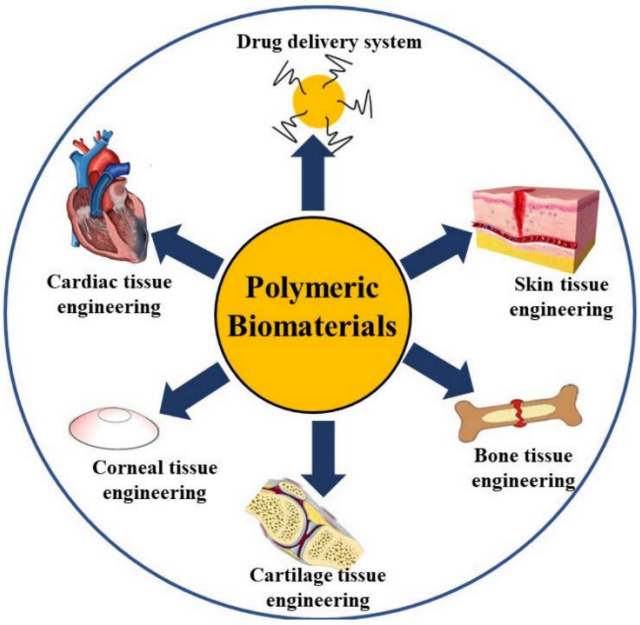


Figure 2.4 The application areas of biopolymers (Kalirajan et al., 2021)

In general, polymers can be divided into three categories: natural, synthetic, and semi-synthetic polymers. Natural polymers are utilized as biomaterials because of their low immunogenicity and biocompatibility. Collagen, fibrin, hyaluronic acid, and keratin belong to the natural group of biopolymers.

Besides natural polymers, synthetic polymers are used in biomedical applications. Also, synthetic biopolymers have better performance for patients with allergic reactions to natural polymers. Moreover, it is known that synthetic polymers have better mechanical properties than natural polymers. Several synthetic polymers, such as alcohol (PVA), polylactic acid (PLA), polyvinyl polycaprolactone (PCL), and polylactic-co-glycolic acid (PLGA), are the most utilized because of their effectiveness in biological contexts (Kalirajan et al., 2021).

Semisynthetic polymers are prepared by combining natural and synthetic polymers by blending, grafting, or crosslinking. Chitosan is an example of a semisynthetic polymer (Gutierrez Cisneros et al., 2021).

### *2.2.3 Metallic Biomaterials*

Due to their strength, metals are commonly used in shape memory alloys, dentistry, maxillofacial implants, joint and bone replacements, and cardiac stents. Ti (titanium) and its alloys, stainless steel, amalgam, Ag (silver), and Pt (platinum) were mostly used as metallic biomaterials (Hermawan et al., 2011). When metals are preferred as biomaterials, they can cause local inflammation or rejection. To prevent this, metals are surface coated with a biocompatible material (Paul, 2019).

### *2.2.4 Biocomposites*

Composites are composed by mixing two or more different materials with highly disparate characteristics. The occurring composites aim to enhance the material's properties in all aspects, including physicochemical, mechanical, and biological aspects. Properties that cannot be achieved with a single material can be reached with composites whose components are selected according to the properties determined for

the application. For example, a composite scaffold consisting of calcium phosphate with PLGA was created to control the degradability of both rapidly degradable PLGA and poorly degradable calcium phosphate (Paul, 2019; Y. Wang, 2016).

## 2.3 Piezoelectric Materials

Piezoelectric materials belong to the class of dielectric materials. Dielectrics are insulating materials that have no free electrons. However, they can be polarized when an external electric field is applied (Khan & Upadhyay, 2021; Vijaya, 2012). The classification of dielectric materials, based on their response to electrical stimuli, is presented in Figure 2.5.

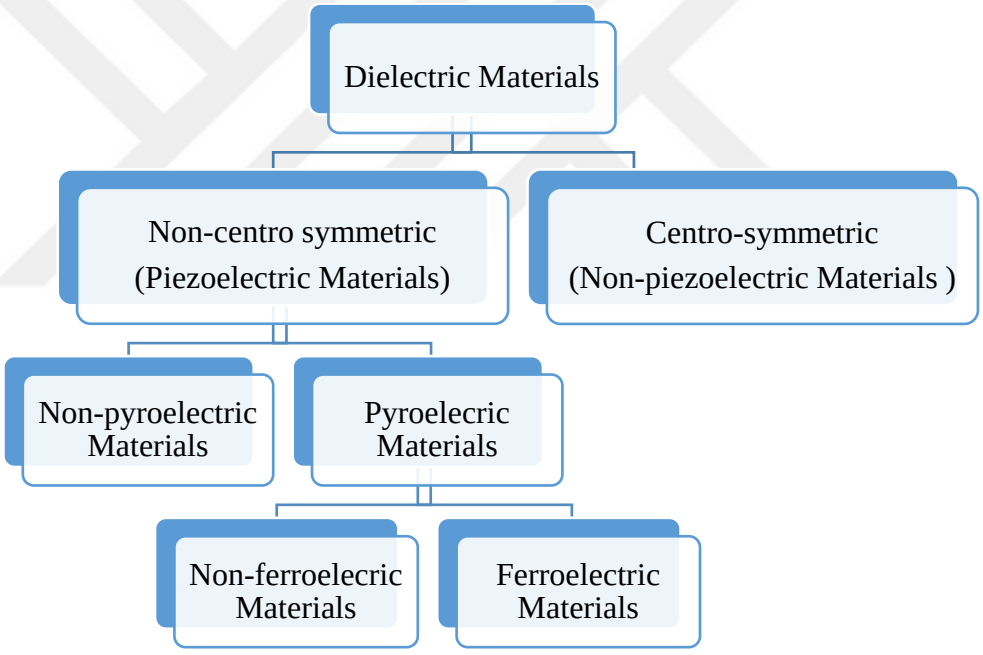


Figure 2.5 Classification of dielectric materials (Khan & Upadhyay, 2021)

There are relationships between piezoelectric, pyroelectric, and ferroelectric materials, and Figure 2.6 visually represents how they are connected. Piezoelectric materials are dielectric that can convert mechanical energy into electrical energy and vice versa. Pyroelectrics are a subclass of piezoelectric that can show polarization changes in response to temperature changes. Ferroelectric materials exhibit

pyroelectric and piezoelectric characteristics, with their permanent polarization being reversible when subjected to an electric field (Khan & Upadhyay, 2021; Vijaya, 2012).

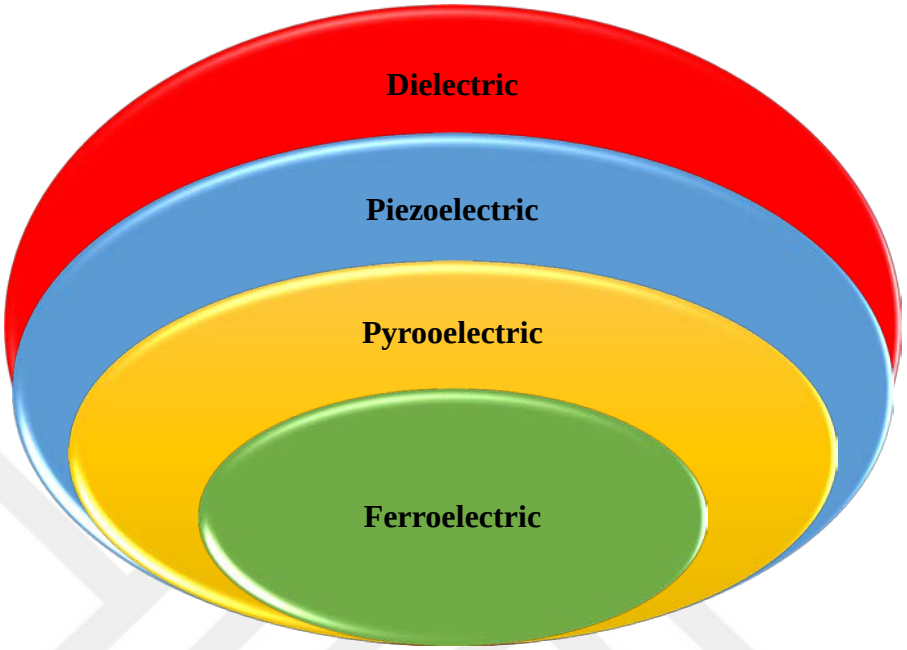


Figure 2.6 Relationship of dielectric, piezoelectric, pyroelectric, and ferroelectric materials(Khan & Upadhyay, 2021)

Piezoelectric materials are dielectric materials that convert mechanical energy into electrical energy (direct piezoelectric effect) or mechanical energy (converse piezoelectric effect). The schematic representation of the direct and converse piezoelectric effect is given in Figure 2.7.

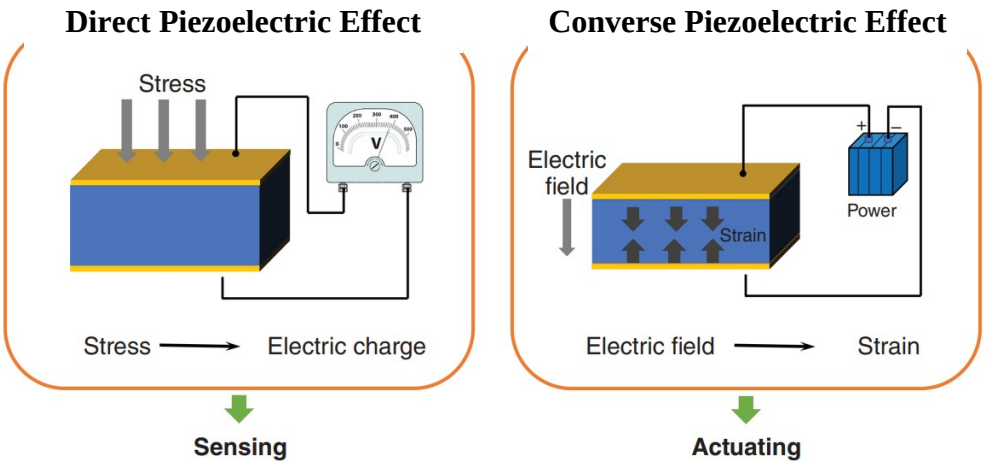


Figure 2.7 The schematic representation of direct and converse piezoelectric effect (J.-F. Li, 2021)

Ferroelectric materials are characterized by their reversibility of permanent polarization under the influence of an electric field. They possess both piezo and pyroelectric characteristics.

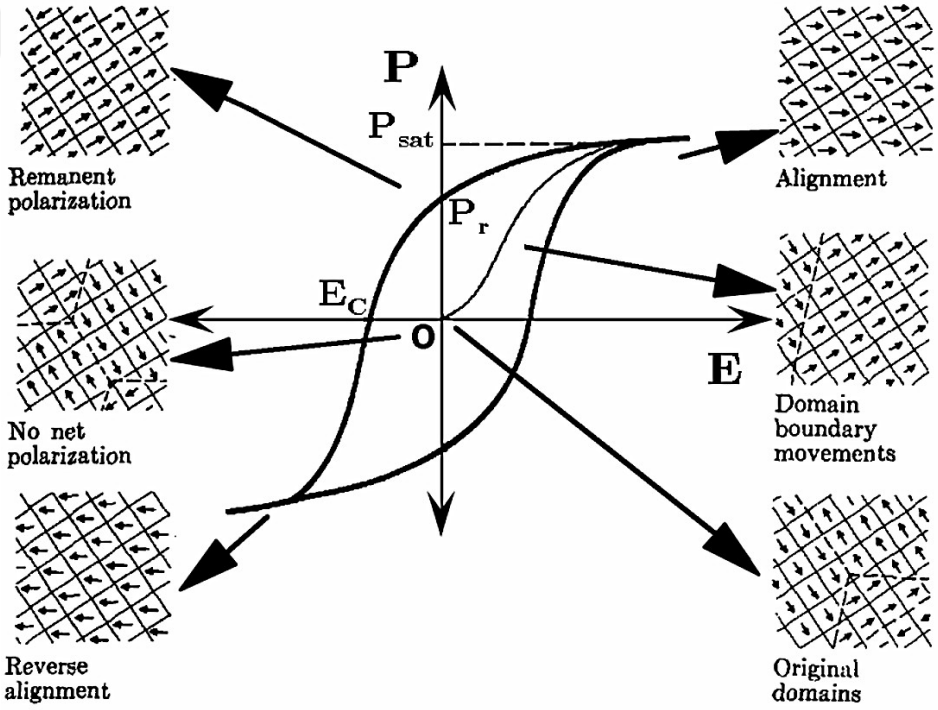


Figure 2.8 Hysteresis loop and domain switching scheme (Kamel, 2007)

A hysteresis loop in ferroelectrics describes the relationship between the polarization and the applied field. Domain switching and hysteresis loop are shown in Figure 2.8. The terms remanent polarization (Pr), coercive field (Ec), and saturation polarization (Ps) are important. While Pr is the polarization value at the zero field (point E), Ec is the required field for depolarization the material to zero polarization. Ps is the maximum polarization point where all dipoles are aligned (Kamel, 2007; Vilarinho, 2005).

Piezoelectric materials have a crystal structure that lacks central symmetry, resulting in small dipoles within their unit cells. The dipoles are randomly oriented under normal conditions. That means the dipoles are oriented in different directions in this condition. However, when piezoelectric materials are exposed to an external and high electric field, they become polarized, and all dipoles are oriented in the same direction. This causes the piezoelectric coefficient of the material to be enhanced. When a material has a piezoelectric property, the magnitude of a material's piezoelectric property is expressed by its piezoelectric charge constant ($d_{33}$) which relates the developed polarization to the applied stress (Cholleti, 2018; Qifeng et al., 2019; Rotan et al., 2020; Sharma et al., 2022; L. Zhang et al., 2014).

The following formulas are used to write the constitutive equations for linear piezoelectric materials at low stress (X). The interaction between the electric field, charge density displacement, stress, and strain of the piezoelectric material is defined by these equations (Bechmann, 1956; Behera, 2021):

$$S = sX + dX \qquad (1)$$

$$D = \varepsilon X + dX \qquad (2)$$

where, S is strain, s is elastic compliance, E is electric field, D is dielectric displacement, and ε is permittivity. All materials are subject to strain with elastic compliance and stress, as shown by the values of sX and εX in the equations. Piezoelectric material attributes exclusively include the second part of the equations

containing the piezoelectric charge constant (d). These equations are crucial when it comes to working with piezoelectric material (Behera, 2021; Vilarinho, 2005).

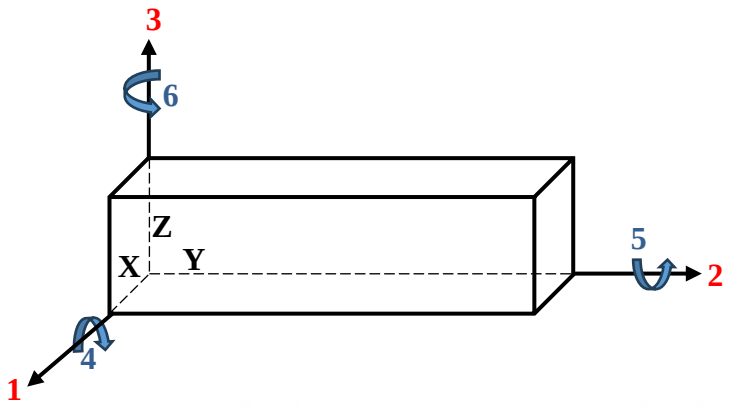


Figure 2.9 The direction of the forces acting on a piezoelectric element (Behera, 2021).

Physical constants in a piezoelectric ceramic are dependent on both the direction of the applied mechanical or electric force and the perpendicular directions to the applied force due to its anisotropic nature. Consequently, each constant generally has two subscripts that show the directions of the two related numbers, such as stress and strain. Typically, the positive polarization direction aligns with the Z-axis in a rectangular coordinate system of X, Y, and Z axes (see Figure 2.9). The subscripts 1, 2, and 3 denote direction X, Y, or Z, respectively, and the subscripts 4, 5, or 6 denote shear about one of these axes (Behera, 2021).

The piezoelectric coefficient d is the constant that describes the linear proportional relationship. It is a third-rank tensor that connects the second-rank tensor (stress or strain) and the first-rank tensor (electric displacement or field). Therefore, the piezoelectric equations can be expressed as follows (i, j, k = 1, 2, 3). The piezoelectric equations can be written in the following form:

$$Dk = dkij + Tij \qquad (3)$$

$$Sij = d^{*}kij + Ek \qquad (4)$$

where *Dk* is electric displacement ($C/m^2$), *Ek* is electric field component (V/m), Sij is strain component, Tij is stress component ($N/m^2$), dkij or $d^*$kij is component of the piezoelectric charge or strain constant (J.-F. Li, 2021).

The piezoelectric coefficient correlates a field along the i-axis to the strain in the j direction. As an example of this explanation, the meaning of some piezoelectric coefficients, such as $d_{33}$, $d_{35}$, and $d_{31}$ is explained below using Figure 2.9. Among these coefficients, $d_{33}$ is the most commonly used of these coefficients and it is the related coefficient for both strain and field along the polar axis (Behera, 2021; Vijaya, 2012).

**$d_{33}$**: Induced strain in direction 3 per unit electric field applied in direction 3, or induced polarization in direction 3 (parallel to the direction of the polarized ceramic element) per unit stress applied in direction 3 (perpendicular to the direction of the polarized ceramic component).

**$d_{35}$**: Induced strain in direction 5 per unit electric field applied in direction 3, or induced polarization in direction 3 (parallel to the direction of the polarized ceramic element) per unit stress applied in direction 5 (perpendicular to the direction of the polarized ceramic component).

**$d_{31}$**: Induced strain in direction 1 per unit electric field applied in direction 3, or induced polarization in direction 3 (parallel to the direction of the polarized ceramic element) per unit stress applied in direction 1 (perpendicular to the direction of the polarized ceramic component).

### *2.3.1 Phase Transition of Piezoelectric*

Ferroelectric materials cease to exhibit their ferroelectric properties once they surpass the Curie temperature (Tc), which is also a point of structural phase transition. It's the temperature where the phase transition occurs. The transition temperatures affected some properties like dielectric constant, optical, thermal and elastic properties of the dielectric materials. Each material has a different Curie temperature. Above the

Tc, the material loses its ferroelectricity and transitions to the paraelectric phase. In other words, domains are randomly oriented in the paraelectric phase (Z. Liu et al., 2023). The material becomes ferroelectric below Tc because of the spontaneous polarization and the interaction between the dipoles.

Figure 2.10 shows the change in dielectric constant and phase transformations as a function of temperature. In this figure, barium titanate has a three-phase transition depending on temperature. It transforms from cubic phase to tetragonal phase at Tc 120 °C, tetragonal to orthorhombic phase at 5 °C, and orthorhombic to rhombohedral phase at −90 °C. Among them, only the cubic phase is not a ferroelectric phase (paraelectric phase), which can't show piezoelectricity (Fu & Itoh, 2015). The transition from the paraelectric to the ferroelectric phase is reversible in terms of its structure (Vilarinho, 2005).

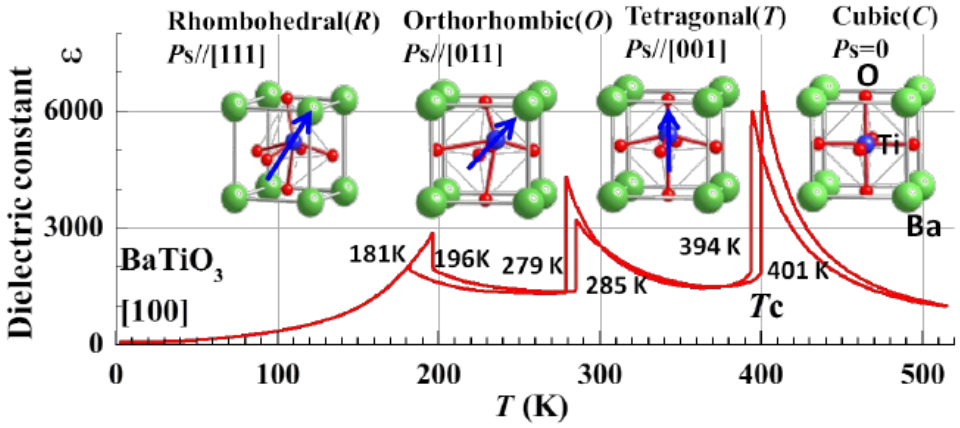


Figure 2.10 Lattice distortion of mono-domain of the $BaTiO_3$ crystal under the application of an electric field (Fu & Itoh, 2015)

Additionally, a material has a phase transition line when it has more than one ferroelectric phase simultaneously. The morphotropic phase boundary (MPB) has the potential to enhance the piezoelectric effect when subjected to stress due to its low energy barrier, resulting in easily orientable polarization properties (C. Wang et al., 2023). It is possible to approach the MPB not only by changing the composition but also by changing the temperature (W. Liu & Ren, 2009).

Lead zirconate titanate (PZT, Pb ($Zr_{1-x}Ti_x$)$O_3$), and lead-free piezoelectric materials such as BCZT (x($Ba(Ti_{0.8}Zr_{0.2})O_3$)-1-x($Ba_{0.7}Ca_{0.3}$)$TiO_3$) have a high piezoelectric coefficient, which has MPB (W. Liu & Ren, 2009; C. Wang et al., 2023)

The phase diagram of the BZT-xBCT system is displayed in Figure2.11(a). This phase diagram was obtained by plotting the dielectric permittivity (***ε***) against temperature curves (T); a few representative ones are displayed in Figure 2.11 (b). The phase diagram exhibits a morphotropic phase boundary (MPB) that emerges from a tricritical triple point involving cubic paraelectric (C), ferroelectric rhombohedral (R), and tetragonal (T) phases. The high piezoelectricity of the MPB compositions comes from their proximity to the tricritical triple point, which causes the polarization anisotropy to almost disappear and allows for easy polarization rotation between the T and R states (W. Liu & Ren, 2009).

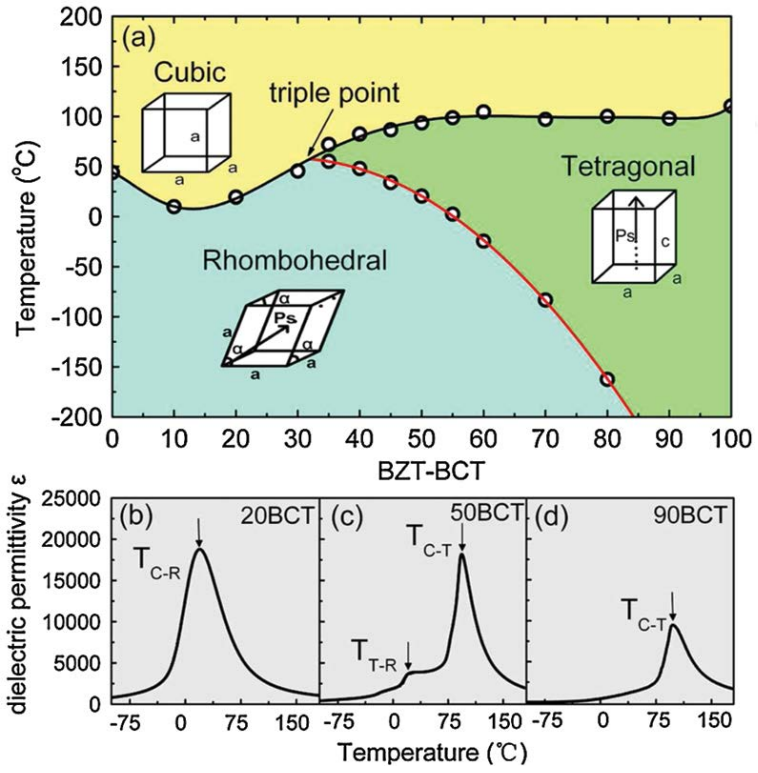


Figure 2.11 (a) The phase transition line of BCZT. (b) Dielectric permittivity curves for different BCT ratio as 20BCT, 50BCT, and 90BCT, respectively (W. Liu & Ren, 2009)

### *2.3.2 Piezoelectric Biomaterials*

The classification of piezoelectric biomaterials according to their $d_{33}$ coefficient is given in Figure 2.12. Piezoelectric biomaterials are broadly categorized into four groups: (i) naturally occurring piezocrystals; (ii) piezoceramics (lead-based, lead-free, and titanate ceramics); (iii) piezopolymers; and (iv) piezocomposites. It should be noted that natural bone is a piezocomposite including minerals and collagen, with a $d_{33}$ coefficient of 0.7 pC / N (Bur, 1976; Kapat et al., 2020). Some examples of piezoelectric materials include PZT: $Pb(Zr,Ti)O_3$, BT: $BaTiO_3$, PT: $PbTiO_3$, BN: boron nitride (BN), GaN: gallium nitride, LN: $LiNbO_3$, LNKN: $Li(Na,K)NbO_3$, KNN: $(K,Na)NbO_3$, PMN: $PbMgNbO_3$, BNT: $(Bi,Na)TiO_3$, ZnO: zinc oxide, HA: hydroxyapatite, PLLA: poly(l-lactic acid), PVDF: poly(vinylidene fluoride), P(VDF-TrFE): poly(vinylidene fluoride-trifluoro ethylene), PHB: polyhydroxybutyrate, FF-PNT: diphenylalanine based peptide nanotubes (Kapat et al., 2020). Among the piezoelectric materials, piezoceramics offers a diverse array of applications, making them an indispensable material.

$BaTiO_3$ is one of the most preferred piezoelectric biomaterials in tissue engineering applications. It is a perovskite ($ABO_3$) material with a $d_{33}$ of about 200 pC/N and a Curie temperature of 120 °C. Moreover $BaTiO_3$; is a material whose piezoelectric properties can be improved by doping various ions such as $Ca^{+2}$, $Zr^{+4}$, and $Sr^{+2}$ (Acosta et al., 2018; Praveen et al., 2014; Puli et al., 2014; Tariverdian et al., 2019). BCZT is one of the materials with improved piezoelectricity by doping $Ca^{+2}$ and $Zr^{+4}$ ions into $BaTiO_3$. While Ca substitutes the position of Ba-site, Ti replaces its place with Zr. This situation generates stress in the lattice, and this distorts to occur in the lattice. Thus, a material with better piezoelectricity than $BaTiO_3$ is produced (W. Liu & Ren, 2009). In this case, BCZT is a biomaterial with a high piezoelectric coefficient, promoting its potential for tissue engineering.

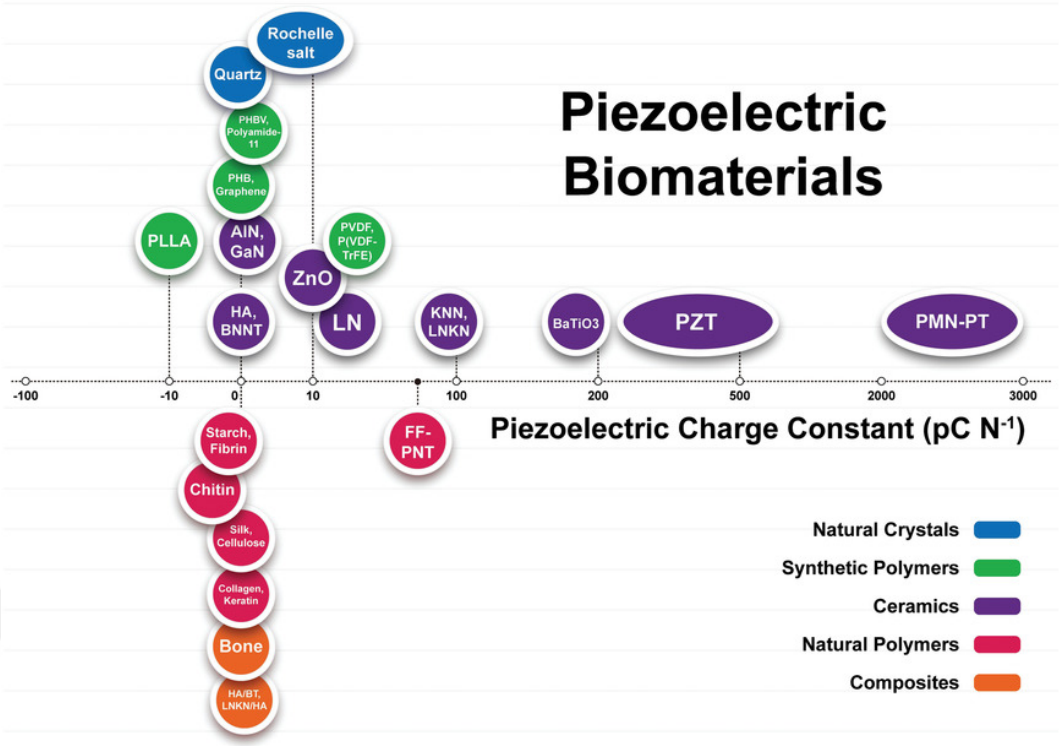


Figure 2.12 Classification of piezoelectric biomaterials based on origin and piezoelectric charge constants ($d_{33}$) (Kapat et al., 2020).

### *2.3.3 Poling Process*

Piezoelectric materials capability to transform a mechanical deformation into an electric signal and vice versa. Piezoelectric materials have a crystal structure that lacks central symmetry, resulting in small dipoles due to the formation of domains within their unit cells. The dipoles are randomly oriented under normal conditions. However, when piezoelectric materials are exposed to an external and high electric field, they become polarized, and all dipoles are oriented in the same direction. This causes the piezoelectric coefficient of the material to be enhanced. Therefore, polarization is an important process for piezoelectric materials (Rotan et al., 2020). Polarization is usually carried out below the Curie temperature and by applying a high voltage. There are contact (conventional) and non-contact polarization systems. The corona method (see Figure 2.10) is a non-contact method (Tansel et al., 2013) that allows the polarization of both powder and bulk materials (Park et al., 2014; Qifeng et al., 2019; Sharma et al., 2022; K. Wang et al., 2022; Y. Zhang et al., 2014). Comparison of conventional and corona method, the powders polarization is not possible with the

conventional poling method, while they can be with the corona method. In addition, since it is a non-contact method, it is very convenient to avoid toxicity in the polarization of biomaterials. It is preferred method in this study.

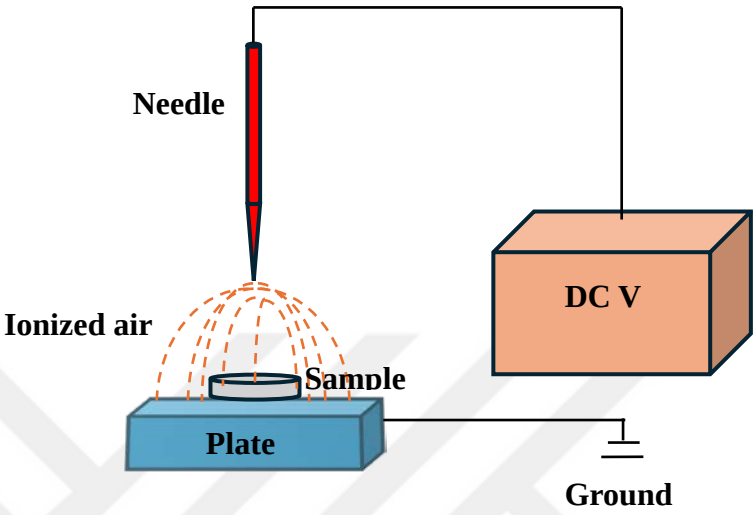


Figure 2.13 Illustration of corona poling method.

The corona polarization system comprises a conical tip needle electrode, a grounded plate on which the sample is placed, a heating plate, and a DC voltage source, as shown in Figure 2.13. The success of the corona polarization system depends on several parameters. These parameters are the applied voltage, the distance between the needle and the sample, the sample thickness, the temperature, and the time the sample is exposed to external electric field (Adamiak & Atten, 2004). It should be noted that the formation of sparks cannot be avoided. Therefore, the maximum voltage is determined first. The corona poling condition is set according to Equation 5 which is given below. E is the electrical field, V is the applied voltage, and d is the distance between needle and plate. All parameters must be optimized to evaluate the effect of different variables.

$$E = \frac{\mathrm{V}}{\mathrm{d}} \qquad (5)$$

The conventional contact polarization method can only be applied to bulk samples. In this method, the samples must be covered with silver paste or gold plating before

polarization. In addition, when using this method, high voltage is usually applied to the sample in heated silicone oil. However, the choice of conventional contact method for polarization of biomaterials may cause a toxic effect. Therefore, the corona polarization system is more suitable for biomaterials than contact methods because it is a non-contact polarization method (Rotan et al., 2020; Sharma et al., 2022).

## 2.4 Bone Substitutes for Orthopedic Surgeries

Bone has the capability of regeneration itself. However, when a bone defect exceeds a critical size, bone cannot regenerate itself. In this case, it requires using substitution materials, which can be natural or synthetic to support bone regenerating cells in this situation (Barba et al., 2018). However, it was noted that the ideal bone substitutional material needs to fulfill several specific criteria such as being osteoconductive, osteoinductive, biocompatible, bioresorbable, structural similarity to the bone, porosity, mechanical resistance, ease of use, safety, and cost-effectiveness (Faour et al., 2011; Fernandez de Grado et al., 2018). Many synthetic substitution materials can support bone repair in bone defects such as bone cement. There are different types of bone cements based on chemical composition origin as given in Figure 2.14. Among them, phosphate-based bone cement is an important and commonly used group in bone tissue applications.

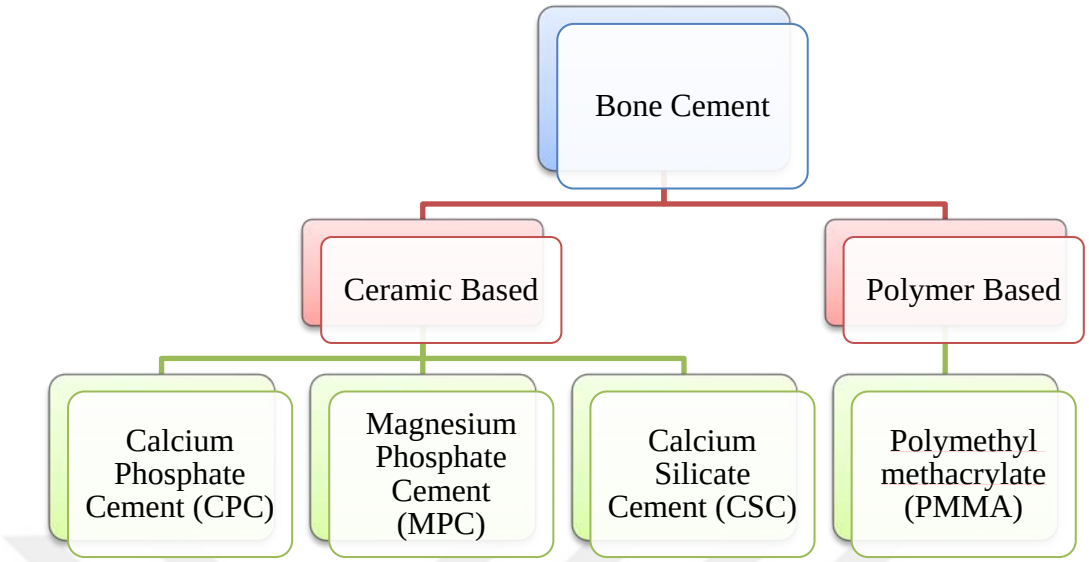


Figure 2.14 Bone cement classification based on chemical composition

### *2.4.1 Phosphate Based Bone Cement*

Bone cement is one of the most preferred bone substitute materials. Especially, they are useful for treating complex bone damage. They can be injected directly into the damaged area through invasive surgery without the need for open surgery. They can easily adapt to bone damage locations and harden in vivo at the site where they are injected. In addition to these benefits, bone cement displays unique properties like biocompatibility and biodegradability (F. Chen et al., 2015; Kim & Jeon, 2012; Şahin & Kalyon, 2017; D. Wang et al., 2014).

Bone cements turn into a viscous form when mixed with water. This viscous mixture can be easily shaped, and strength can be achieved quickly as it can harden spontaneously through several hydration reactions. Phase transformation based on precipitation and dissolution activities leads to cement paste setting and hardening. When the hydrophilic cement particles are hydrated in water, a chemical reaction between cement and water begins. This hydration process, like that occurring in Portland cement, leads to hardening so that the cement has an enhanced mechanical strength over time, called setting process. Moreover, the chemical composition of cement influences the chemical reactions during the setting process. In most cases, the

addition of particles without setting capability affects the setting process of the injectable bone scaffold, resulting in delayed setting time but enhancing injectability (T. Wu et al., 2023).

Phosphate-based bone cement is a great tool for mimicking natural bone owing to its similar mineral structure. Among them, calcium phosphate cement (CPC) and magnesium phosphate cement (MPC) stand as pivotal components for bone repair and regeneration.

The use of CPC as a bone repair biomaterial in clinics has been successful for several years. If CPC is used as an injectable paste can harden in vivo and transform into the ultimate product, which is hydroxyapatite (HA) represented by the chemical formula $Ca_{10}(PO_4)_6(OH)_2$. This is the main compound in the mineral phase of bone and teeth. Because of its excellent compatibility, ability to trigger bone growth and potential for replacing bone, CPC shows great promise for various clinical applications (Burguera et al., 2006; Jeong et al., 2019; Kim & Jeon, 2012; F. Wu et al., 2008). Nevertheless, the limited mechanical properties and slow biodegradation rate restrict its potential for other uses (Ambard & Mueninghoff, 2006; Ishikawa, 2014; F. Wu et al., 2008).

On the other hand, the properties of MPC include fast setting, high initial strength, and comparatively quick in vivo degradation. The main constituents of MPC are ammonium dihydrogen phosphate ($NH_4H_2PO_4$) and dead-burnt magnesia (MgO). Struvite, or $NH_4MgPO_46H_2O$, is the final product of the reaction between the MPC powders and water. Also, besides struvite phase, it is possible to obtain minor phases such as schertelite, $(NH_4)_2Mg(HPO_4)_2 .4H_2O$ and dittmarite, $MgNH_4PO_4 .H_2O$ (Qiao et al., 2009; F. Wu et al., 2008).

When water is mixed with magnesia and phosphate powder, the phosphate quickly dissolves, creating an acidic water solution. This is followed by the dissolution of magnesia, which releases magnesium ions into the solution. Then the crystalline products are formed due to intense chemical reactions. The structure of magnesia plays a crucial role in determining the performance of MPC, particularly its setting time. This structure is influenced by several factors, including the temperature and duration

of the calcination process, the grinding method employed, and even the choice of precursor material used in the production of magnesia. In general, as the calcination temperature increases, the reactivity of magnesia decreases. Increasing the surface area results in higher reactivity and faster reaction rates (Birchal et al., 2000; Bocanegra-Bernal, 2008; Qiao et al., 2009; Soudée & Péra, 2000, 2002)

An exothermic reaction occurs between acid phosphate and basic magnesia in MPC cement. Because of the exothermic reaction, the setting reaction occurs in less than 3 min. However, this time is not suitable for any application, especially for bone tissue engineering. For this reason, controlling the exothermic chemical reactions is essential for MPC. To delay the setting time of MPC, a key is the decreased reactivity of magnesia (Qiao et al., 2009). Decreasing the reactivity of magnesia is possible by using high temperature for calcination of it. Magnesia can be classified as lightweight, hard-burned, and dead-burned. The classification details are given below (Al-Tabbaa, 2013; Shand, 2006):

**Lightweight magnesia:** It is produced at a temperature of ~700-1000°C. It is used in plastics, rubber, paper, and pulp because it has the highest reactivity, the least crystallinity, and the largest surface area.

**Hard-burned magnesia:** It is fabricated at a temperature of ~1000-1400°C. It has been used in animal feeds and fertilizers since it has intermediate properties.

**Dead-burned magnesia (Periclase):** It is manufactured at temperatures of ~1400-2000°C. It is used extensively in refractory applications. It possesses the lowest surface area, the highest crystallinity, and the least reactivity.

Among these magnesia types, using dead-burned magnesia can be a good choice for bone cement preparation. It has the least reactivity; therefore, it can delay the setting time by avoiding an exothermic reaction. The other way to delay setting time may be to make a composite with a material that has a longer setting time, such as CPC.

CPC and MPC have advantages and disadvantages when they are used alone. It was thought that their combination could produce a calcium-magnesium phosphate cement

(CMPC) with improved properties. Wu et al., in 2008, and Chen et al. in 2015 prepared a composite including CPC and MPC. They obtain better setting time and compressive strength properties by using CMPC (F. Chen et al., 2015; F. Wu et al., 2008).

## 2.5 Desired Property for Bone Cement

The following is a list of the desired properties that bone cement should have. All of these criteria should be met by an "ideal" cement; however, there is no such thing as "ideal" bone cement, and all the bone cements that is currently in use has some drawbacks (Ginebra, 2009).

- **Ease of handling**
- **Injectability**
- **In vivo setting and hardening with appropriate setting times**
- **Low setting temperature**
- **Near neutral pH during setting**
- **No disintegration in early contact with body fluids**
- **No shrinkage during setting**
- **Appropriate mechanical strength**
- **High radiopacity**
- **No toxicity**
- **Biocompatibility**
- **Bioactivity**
- **Porosity**

Among these desired properties, injectability, setting time, and compressive strength were explained in sections 2.5.1, 2.5.2, and 2.5.3.

### *2.5.1 Injectability*

The injectability of the cement paste is influenced by many factors, including (i) the average particle size and distributions of starting powders; (ii) the agglomeration tendency of the particles; (iii) particle shape; (iv) the powder-to-liquid ratio (P/L); and (v) the presence of additives with specific roles and/or rheological modifiers (Tariq et al., 2019). These factors should be optimized to obtain good injectability. Among them, P/L is the important parameter defined as the use of liquid quantity for a specific mass of powder. Suppose the paste is not prepared according to the appropriate P/L ratio. In that case, phase separation may occur, where the liquid moves faster than the powder during injection, or a non-injectable paste with a high solid content may be obtained.

### *2.5.2 Setting Time*

During the mixing of solid and liquid components of the paste, a physicochemical reaction which involves dissolution, precipitation, and finally phase transformation occurs. When the hydrophilic cement particles are hydrated in water, a chemical reaction between cement and water begins. This hydration process, similar to that occurring in Portland cement, leads to hardening so that the cement has an enhanced mechanical strength over time. Moreover, the chemical composition of cement influences the chemical reactions during the setting process. In most cases, the addition of particles with no setting capability affects the setting process of the injectable bone scaffold, resulting in delayed setting time but enhancing injectability (T. Wu et al., 2023).

When the setting reactions are finished the cement is hardened. Therefore, bone cement's injection process must be finished before hardened cement. Initial ($t_i$) and final ($t_f$) setting times are crucial in clinical applications. The initial and final setting times are the periods required for the setting cement to withstand static pressures of 0.3 MPa and 5 MPa, respectively. Bone cement should be applied to the damaged area before the initial setting time and the wound should be closed after the final setting

time. In orthopedic applications, the $t_i$ value should be close to 8 minutes and the $t_f$ value should be less than 15 minutes (Jansen et al., 2005; Şahin & Kalyon, 2017).

### *2.5.3 Compression Strength*

Bone scaffolds are designed to support the healing of damaged bone tissue. Therefore, tissue scaffolds should resemble natural bone in many aspects such that they should also be compatible with the mechanical properties of the area in which they are used. The bones in the human body exhibit different mechanical properties depending on their structure and function. These mechanical properties are typically expressed in terms of compressive strength. The compressive strength values of the different bone types are as follows: human trabecular bone (30 MPa) (Jansen et al., 2005), cortical bone (90 to 209 MPa), and cancellous bone (1.5 to 45 MPa) (Ginebra, 2009).

# CHAPTER THREE
# MATERIALS AND METHODS

The main purpose of this thesis is to develop injectable bone cement with piezoelectric properties. For this purpose, bone cement containing calcium phosphate cement (CPC), magnesium phosphate cement (MPC), and piezoelectric barium calcium zirconium titanate (BCZT) were mixed. The production and determination of the features of the piezoelectric bone cement are shown as a scheme in Figure 3.1. Also, the experimental details are given in the sections below.

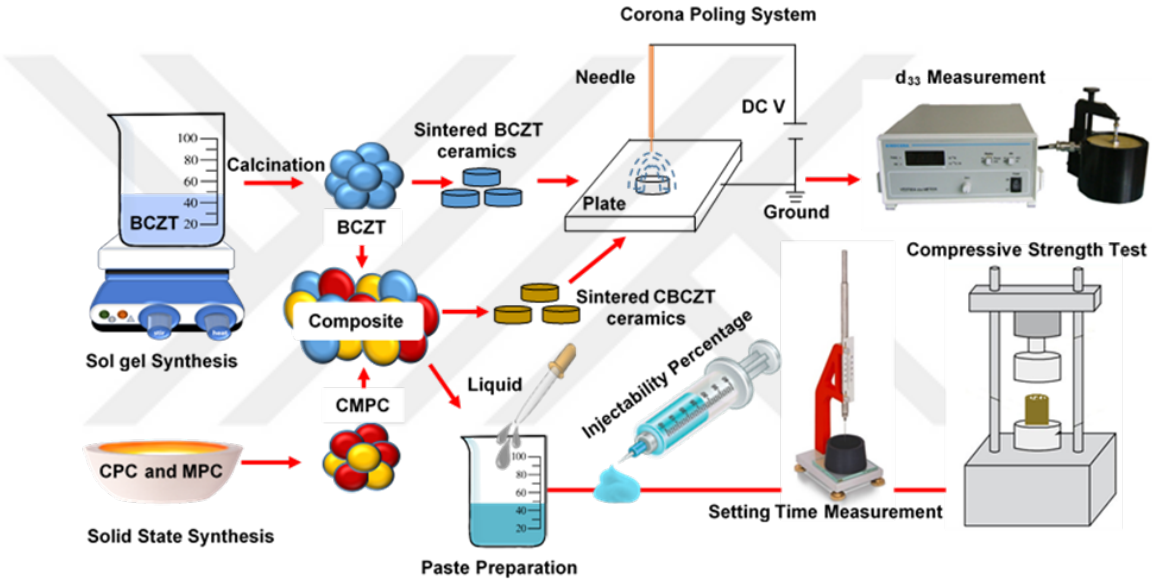


Figure 3.1 The scheme for general production and feature determination steps of this thesis (Sakar et al., 2024)

## 3.1 Powder Fabrication

### *3.1.1 BCZT Synthesis*

The $xBa(Zr_{0.2}Ti_{0.8})O_3$-$(1-x)(Ba_{0.7}Ca_{0.3})TiO_3$ ($x = 0.5$) piezoelectric ceramic powder was synthesized using a sol-gel process with analytical reagent (AR) grade chemicals from Sigma Aldrich. The production details are given as a flow chart in Figure 3.2.

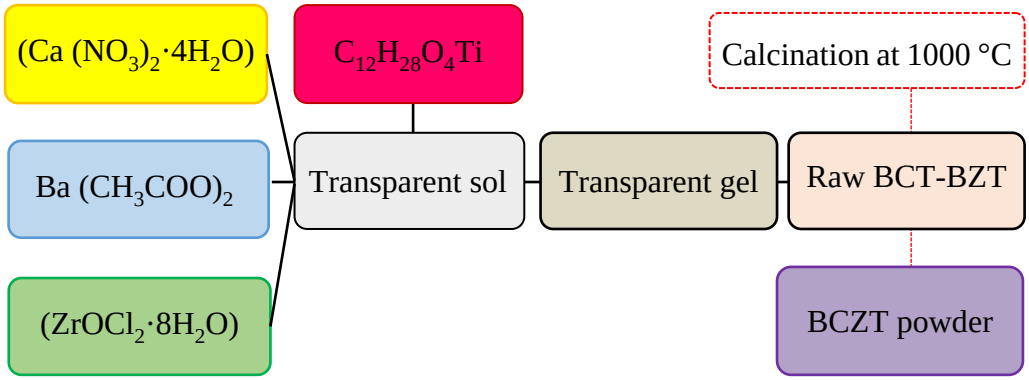


Figure 3.2 The flow chart of BCZT production steps

The required quantity of precursors including barium acetate ($Ba(CH_3COO)_2$), zirconium oxychloride ($ZrOCl_2.8H_2O$), calcium nitrate tetrahydrate ($Ca(NO_3)_2.4H_2O$), and titanium isopropoxide ($C_{12}H_{28}O_4Ti$) were combined in stoichiometric ratios. Barium acetate was dissolved in acetic acid, while zirconium oxychloride and calcium nitrate tetrahydrate were dissolved in ethanol. Each solution was prepared separately and then mixed. Next, titanium isopropoxide was added to the mixture in the appropriate quantity. The resulting precursor solution was heated to 100 °C and stirred continuously for about 4 hours, to obtain precipitated gel. Following the procedures in the literature, first, the gel was dried in an oven for 12 hours, then calcined at 1000 °C for 4 hours in ambient air to form crystalline powders. (Chandrakala et al., 2016; Praveen et al., 2015).

### *3.1.2 CMPC Preparation*

CMPC powders were obtained from equivalent weight ratios of CPC and MPC. Tetracalcium phosphate ($Ca_4P_2O_9$, TTCP) and calcium phosphate anhydrous ($CaHPO_4$, DCPA) are combined in an equivalent molar ratio to produce CPC. The primary materials to produce TTCP were calcium carbonate ($CaCO_3$, Sigma Aldrich) and diammonium phosphate ($(NH_4)_2HPO_4$, Sigma Aldrich), combined in a 1:2 molar ratio. The mixture was transferred to an alumina crucible and heat-treated, by Protherm PTF model tube furnace, at 1500 °C after being crushed for a while in an agate mortar. It was then quenched following a fifteen-hour holding period. On the other hand,

DCPA was obtained by heat-treating calcium phosphate dehydrates ($CaHPO_4.2H_2O$) for four hours at 350 °C. The flow chart of CPC production is given in Figure 3.3.

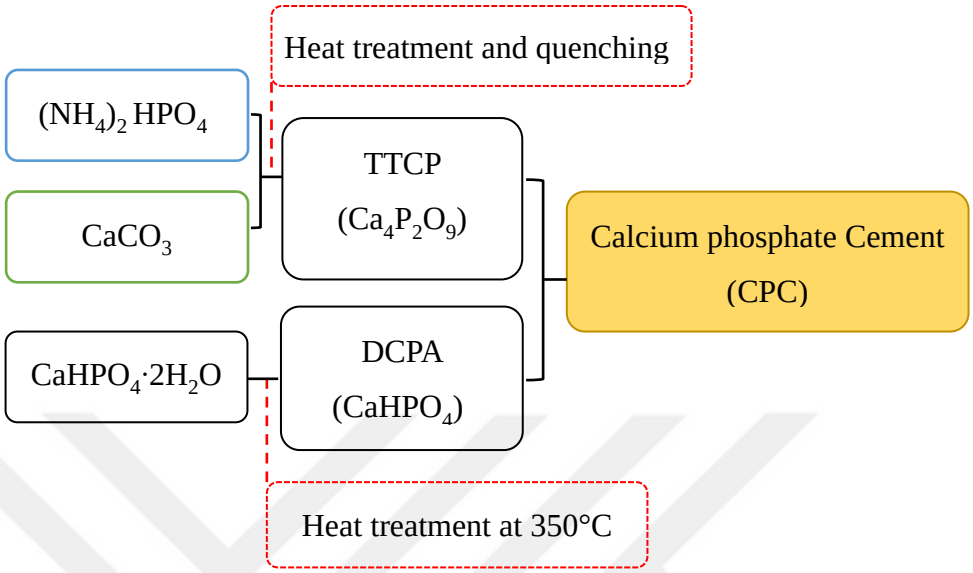


Figure 3.3 The flow chart of CPC production

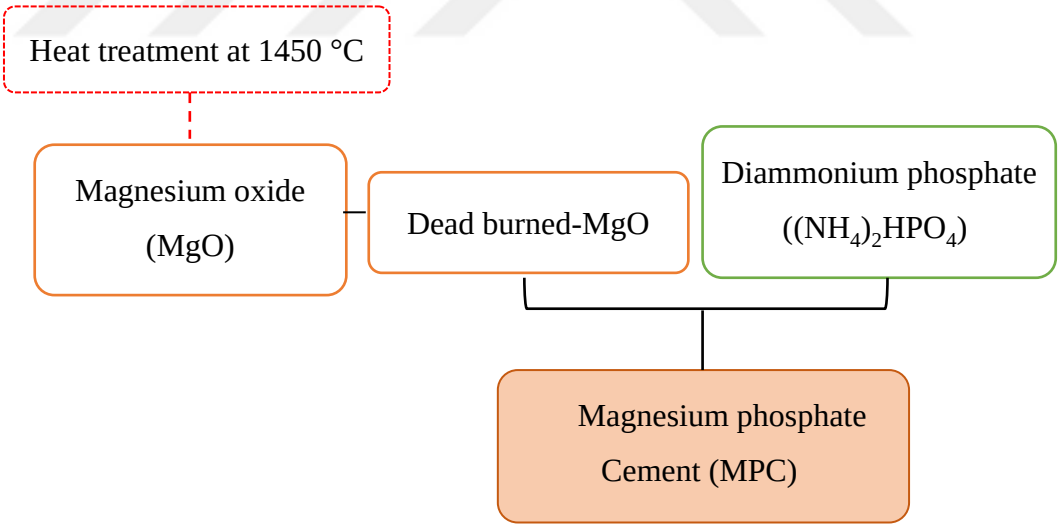


Figure 3.4 The MPC production flow chart

MPC was prepared by mixing dead-burned magnesium oxide and diammonium phosphate ($(NH_4)_2HPO_4$, Sigma Aldrich) in a 3.8:1 molar ratio. Dead-burned MgO

was obtained by heat-treated magnesium oxide (light, %96, Alfa Aesar) at 1450 °C for 4 hours. The flow chart is given in Figure 3.4 which belongs to MPC production.

### *3.1.3 BCZT-CMPC Composite Preparation*

The composites were prepared by mixing CMPC with BCZT powders in different weight percentages (0% CMPC, 20% CBCZT20, 30% CBCZT30, 40% CBCZT40, and 100% BCZT). The pellet samples were fabricated to measure the dielectric constant and piezoelectric coefficient. Polyvinyl alcohol (PVA), a binder, was added to the powder mixtures at a weight percentage of 2.0% (w/w). Pellets were formed by pressing the mixtures containing the binder at 300 MPa using a 10 mm die. After shaping pellets, two step heating treatment was applied to them. While the first step of heat treatment is a binder burn-out, and following step is sintering. For de-binding, the heating regime was optimized initially. 500 °C for 120 minutes at a rate of 1 °C/min was chosen for the first. Then the binder was burned out at a temperature of 600 °C for 60 minutes at a rate of 1 °C/min. Compared to the samples, the specimens heat treated at 600 °C appeared flatter and good. The other specimens, which heat treated at 500 °C were deformed. Therefore, the heat treatment regime of the burn-out process was optimized at 600 °C for 60 minutes at a rate of 1 °C/min.

Following burn-out, the BCZT pellets were sintered at 1450 °C for 180 minutes at a heating rate of 2 °C/min, while the CMPC, CBCZT20, CBCZT30, and CBCZT40 pellets were sintered at 1100 °C for 90 minutes. The density of the sintered samples was measured by using Archimedes' method.

To induce their piezoelectric responses, the sintered pellets were then polarized by a homemade corona poling system which presented details of the method in Figure 3.5. To optimize poling condition different parameter such as needle-plate distance, applied voltage, formation of spark, and the temperature were used. First, the maximum electrical field value (kV/cm) was determined without spark formation, according to the Equation 1 (E=V/d). E value is determined maximum 7.5 kV/cm, d value is 2 cm, so according to the Equation 1, V value must be 15 kV. The poling time was chosen as 2.5 hours. The poling process was carried out at room temperature (RT).

Corona poling was also applied to both the silver paste-electroded and non-electroded samples.

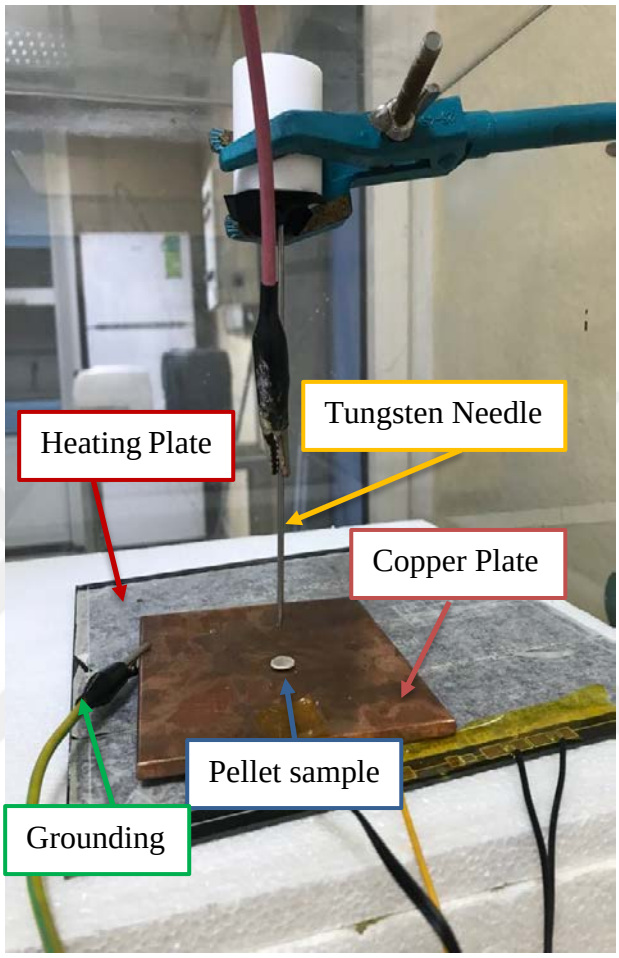


Figure 3.5 A housemade corona poling system (personal Archive, 2023)

## 3.2 Characterizations

Phase analysis of the powder and pellet samples was performed using a Rigaku D/Max (2200/RC Model) X-ray diffractometer (XRD) with Cu-Kα radiation (1.5406 Å) of 2 °C/min in the range of 20° to 80°. The peak data obtained from the XRD pattern was assessed using the X'Pert Highscore Plus program. Gsas software was also utilized to refine BCZT. The morphologic structure was investigated using ZEISS EVO H15 scanning electron microscope (SEM). The particle size distribution was obtained using a Horiba LA-950 particle size analyzer. The dielectric constant and

loss variation with frequency were examined using an E4980AL LCR meter (Keysight Technologies, Santa Clara, CA, USA) at RT, using the sample holder (aixACCT, TFA 423-7). The measurement was controlled with a LabVIEW program. TF analyzer (aixACCT TF Analyzer 1000, Aachen, Germany), in conjunction with a high-voltage amplifier (TREK 610E, TREK, Medina, NY, USA) and laser-interferometer (SIOS Meßtechnik GmbH, Germany), was used to generate polarization and strain loops under the alternating electric field, which was in the form of a triangular wave with a 10 Hz frequency. The samples were corona poled and then analyzed using a $d_{33}$ meter (Sinocera Piezoelectronics, YE2730A, China) to determine the piezoelectric coefficient ($d_{33}$), in which the applied force has an amplitude of 0.25N with 110 Hz frequency. Besides crystal structure and electrical characterizations, the composite cements were evaluated for their injectability, setting time, and compressive strength using the following studies.

### 3.3 Paste Preparations

The powder-to-liquid ratio (P/L), the amount of liquid used for a given mass of powder, is a crucial factor affecting the samples' compressive strength, injectability, and setting time. Different P/L ratios between 1-1.7 g/ml were studied for the optimization. At a minimum, the P/L ratio was set to allow the target injectability value of 70% to be achieved. Therefore, it was the appropriate injectable percentage was obtained with P/L ratio of 1.55 g/ml. Injectable pastes were made by combining powders of CBCZT20, CBCZT30, CBCZT40, and CMPC (control sample) with a liquid solution. The liquid solution was prepared by mixing deionized water and 3.0 wt% polysorbate 80 (Tween 80, Sigma Aldrich).

### 3.4 Injectability Test

The powder and liquid were mixed for 3 minutes using a spatula and then transferred to a 2.5 ml disposable syringe with an internal nozzle diameter of 5.0 mm for an injectability test. Until no paste remained in the syringe, the paste was manually injected. The percentage of injectability was calculated by dividing the weight of the

paste extruded through the syringe by the original weight of the paste in the syringe using Equation 2. The average value was obtained by performing each test three times.

$$\mathrm{INJ} = \frac{\mathrm{Winjected}}{\mathrm{Wtotal}} \times 100 \qquad (2)$$

### 3.5 Setting Time

ASTM Test Method C 187–98 measured the setting time with a Vicat apparatus and the samples after the Vicat test (see Figure 3.6). The Vicat apparatus consists of a frame that holds a 300 g rod and a 1 mm diameter stainless steel needle. The cement samples were removed at 1.0 min intervals from the 100% relative humidity environment and positioned under the 1 mm needle point. The cement samples were periodically removed from a 100% relative humidity environment for 1.0 minute and placed under the 1mm needle point. When the needle was 1 mm above the bottom, the initial setting time (ti) was recorded; when the needle penetrated the cement less than 1 mm, the final setting time (tf) was determined. The average values were calculated after each experiment was repeated three times.

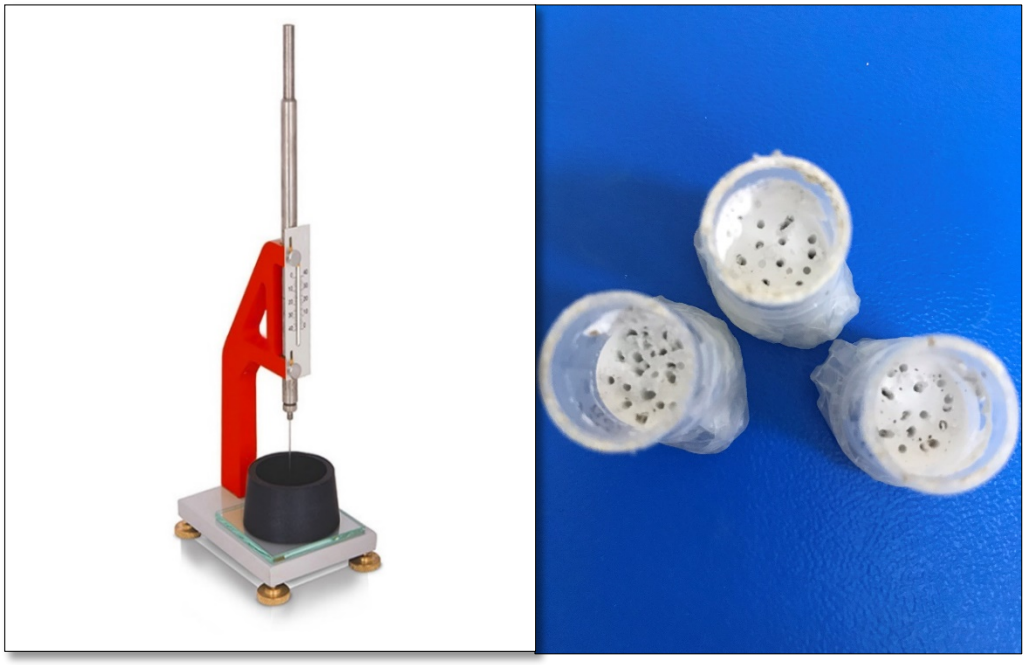

Figure 3.6 Vicat apparatus and the sample after setting time measurement

## 3.6 Compressive Strength

The pastes CBCZT20, CBCZT30, CBCZT40, and CMPC (prepared using the P/L ratio for injectability and setting time) were picked with a spatula and molded into a Ø10×15 $mm^3$ handmade mold by using a 5 ml disposable syringe, as given Figure 3.7. The handmade mold was prepared by cutting the nozzle part of the syringe. Following this, the molded samples were placed in Ringer's solution (0.9 wt.% NaCl) at 37 °C, simulating the saline content of the human bodily fluid, and left to harden for 24 hours. After removal from the solution, the hardened samples were allowed to dry overnight at room temperature. We conducted the same procedure for 72 and 168 hours on CMPC and CBCZT30 to observe time-dependent changes in mechanical behavior. A universal testing machine (AG-2000A, Shimadzu Autograph, Shimadzu Co. Ltd., Japan) was used to evaluate the compressive strength of the specimens at a loading rate of 1 mm per minute. Three replications of each sample group were utilized to assess the results, which were reported as means ± standard deviation (means ± SD).

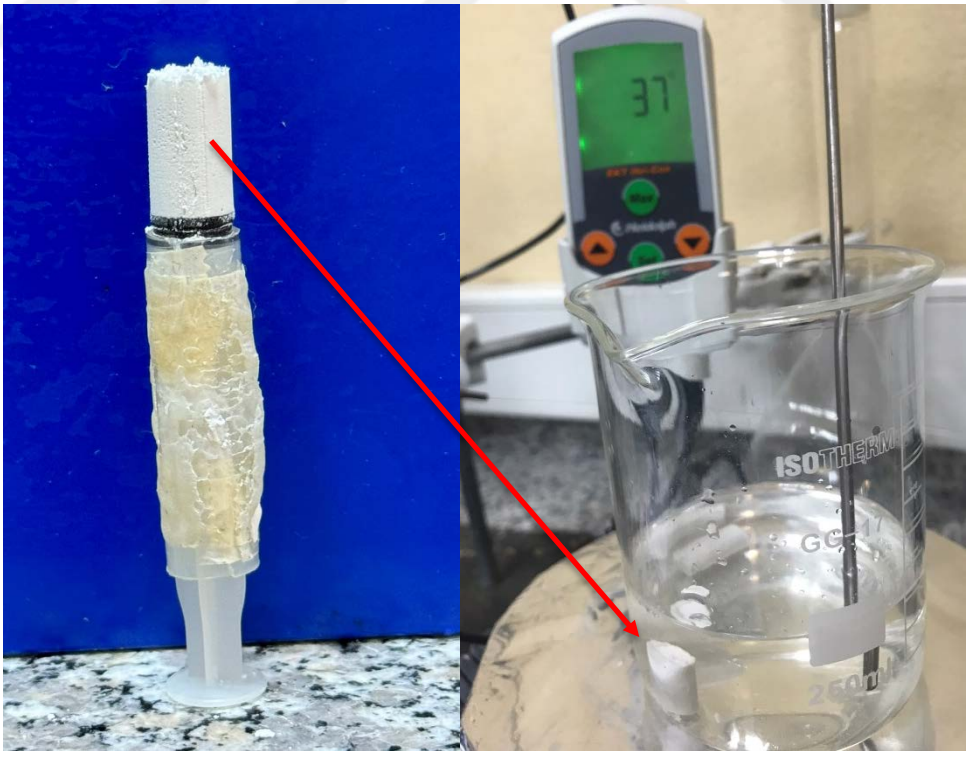


Figure 3.7 The sample preparation of the compressive strength test (Personal Archive, 2023)

# CHAPTER FOUR
# RESULTS AND DISCUSSIONS

## 4.1 XRD Phase Analysis

Figure 4.1 displays the XRD patterns for the BCTZ ceramic and powder. Tetragonal and orthorhombic phases are not prominently seen in the XRD pattern of BCZT, possibly due to their coexistence. Nonetheless, orthorhombic (Amm2, 01-081-2200) and tetragonal (P4mm, JCPDS: 01-075-2120) phases are confirmed to coexist in BCZT powders and ceramics by Rietveld refinement (Figure 4.2). The splitting at approximately 45° is attributed to the orthorhombic ($(022)_{O}$/(200)) and tetragonal ($(200)_{T}$/$(002)_{T}$) phases, like those described in the literature (Patra et al., 2018; Raj et al., 2021b, 2021a; X. Wang et al., 2022). Besides, the formation of triplet $(004)_{O}$/$(040)_{O}$/$(222)_{O}$ at about 66° displays the presence of the orthorhombic phase (Bijalwan et al., 2021), and the peak splitting of $(202)_{T}$/$(220)_{T}$ affirms the tetragonal phase of BCZT (Yan et al., 2022). The splitting of the peaks at 45° and 66° are given in the inset images of Figure 4.1. The lattice parameters obtained by Gsas are shown in Table 4.1 and the fitted refinement graph is indicated in Figure 4.2.

Table 4.1 Rietveld refinement results of BCZT ceramics

| $R_{wp}$, GOF, $\chi^2$ | 15.49%, 1.91, 3.65 | |
|---|---|---|
| Crystallographic system<br>Space group | Tetragonal<br>*P4mm* | Orthorhombic<br>*Amm2* |
| Weight fraction (%) | 66.3 | 33.7 |
| *a* (Å) | 3.9942(6) | 3.9972(8) |
| *b* (Å) | 3.9942(6) | 5.6720(2) |
| *c* (Å) | 4.0082(2) | 5.6765(8) |
| Unit cell volume ($Å^3$) | 63.932 | 128.703 |
| Tetragonality (*c*/*a*) | 1.0035 | |
| Density ($g/cm^3$) | 5.791 | 6.648 |

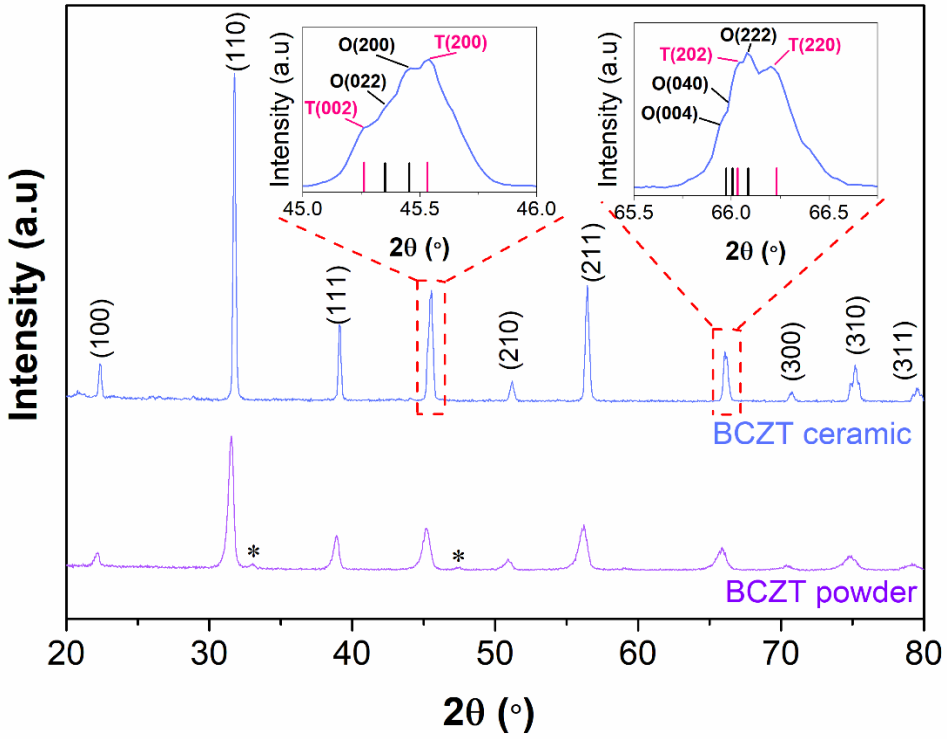


Figure 4.1 XRD patterns of the BCTZ powder and ceramic. The insets show the magnified area at 45° and 66°. * Symbol refers to the $CaTiO_3$ impurity phase

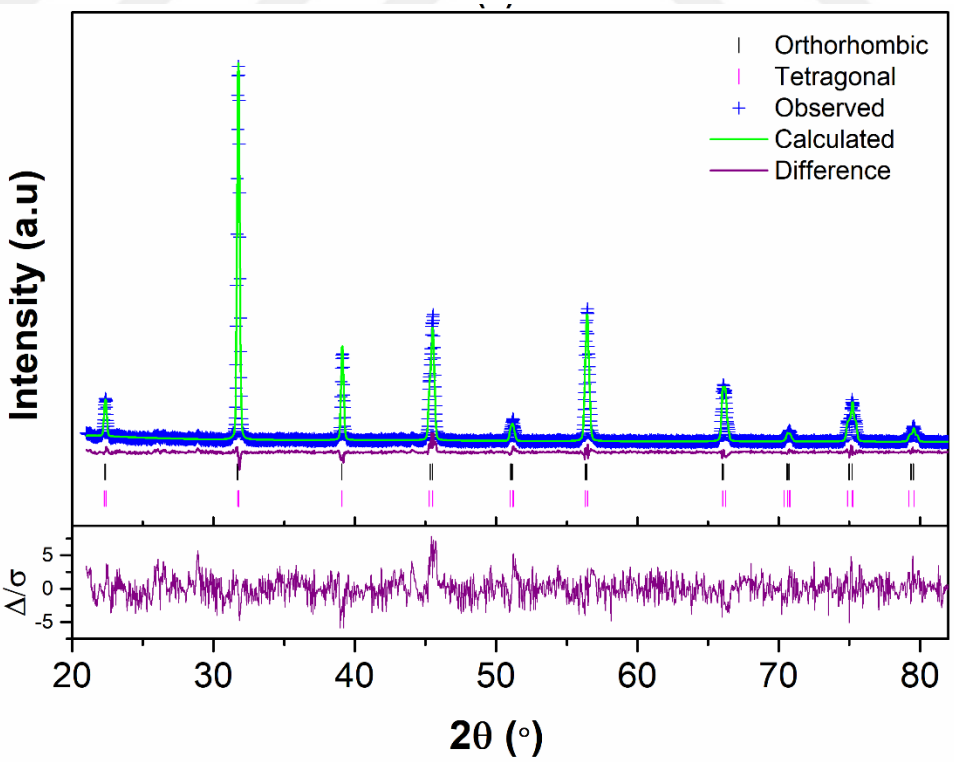


Figure 4.2 Fitted BCZT ceramic diffraction patterns obtained by Rietveld refinement

The powders calcined at 1000 °C show just a trace amount of impurity (marked with the symbol ∗), and the impurity phase is attributed to the orthorhombic $CaTiO_3$ phase (JCPDS:01-082-0229)(W. Li et al., 2012). Nevertheless, the impurity phase entirely disappeared and a pure perovskite BCZT phase occurred when the BCZT pellet samples were sintered at 1450 °C. This showed that the impurity phase diffused into BCZT lattices and, formed a solid solution by sintering at 1450 °C (P. Wang et al., 2011). Moreover, as given in the inlet of Figure 4.1, the splitting of the peak at about 45°, which is related to the orthorhombic and tetragonal phases of BCZT, indicated that $Ca^{2+}$ ions successfully occupied Ba-sites, and $Zr^{4+}$ ions occupied Ti-sites (Tang et al., 2020; D. Wang et al., 2014).

Figure 4.3 displays the XRD patterns of the prepared composite powders before sintering. MgO (Periclase, JCPDS:00-045-0946), $Ca_4P_2O_9$ (TTCP, JCPDS:00-025-1137), $(Ca_3PO_4)_2$ (TCP, JCPDS:01-070-0364), and $CaHPO_4$ (JCPDS: 01-070-0360) are prominent phases in all the composites. All XRD patterns of the composites show the presence of BCZT peaks, except for CMPC, which aligns with expectations.

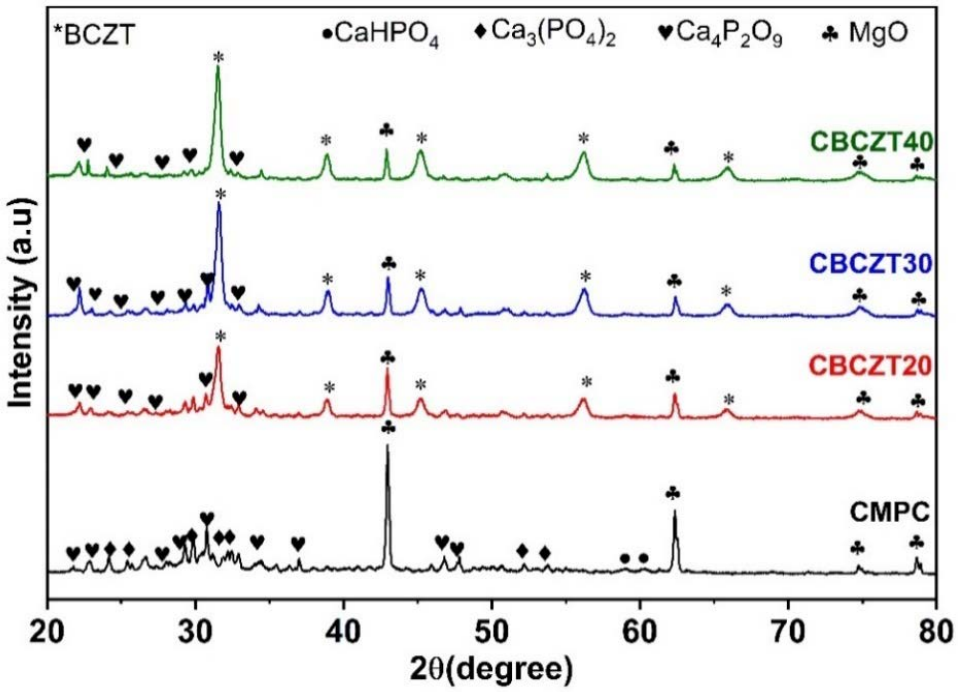


Figure 4.3 XRD patterns of CMPC, CBCZT20, CBCZT30 and CBCZT40 composite powders before sintering showing multiple phases

Based on the XRD results depicted in Figure 4.4, it is evident that the sintered pellet samples display multiphase structures. CMPC contains periclase (MgO, JCPDS:00-045-0946), whitlockite ($Ca_{2.589}Mg_{0.411}O_8P_2$, JCPDS:01- 087-1582), stanfieldite ($Mg_3Ca_3(PO_4)_4$, JCPDS:01-073-1182), and hydroxyapatite (HA, $Ca_5HO_{13}P_3$, JCPDS:01- 072-1243) phases. The XRD pattern of BCZT in CBCZT20, CBCZT30, and CBCZT40 composites aligns well with the JCPDS:01-079-2264, confirming the consistency of the composites.

Figure 4.4 illustrates a decrease in the intensity of the main CMPC peak at ~43º upon BCZT addition in the composites. Upon completion of the sintering process, the CPC and MPC phases underwent a combination resulting in the formation of the whitlockite and stanfieldite phases. However, no new phase formation was observed between BCZT and CMPC, suggesting that BCZT may play a piezoelectric role in the composites.

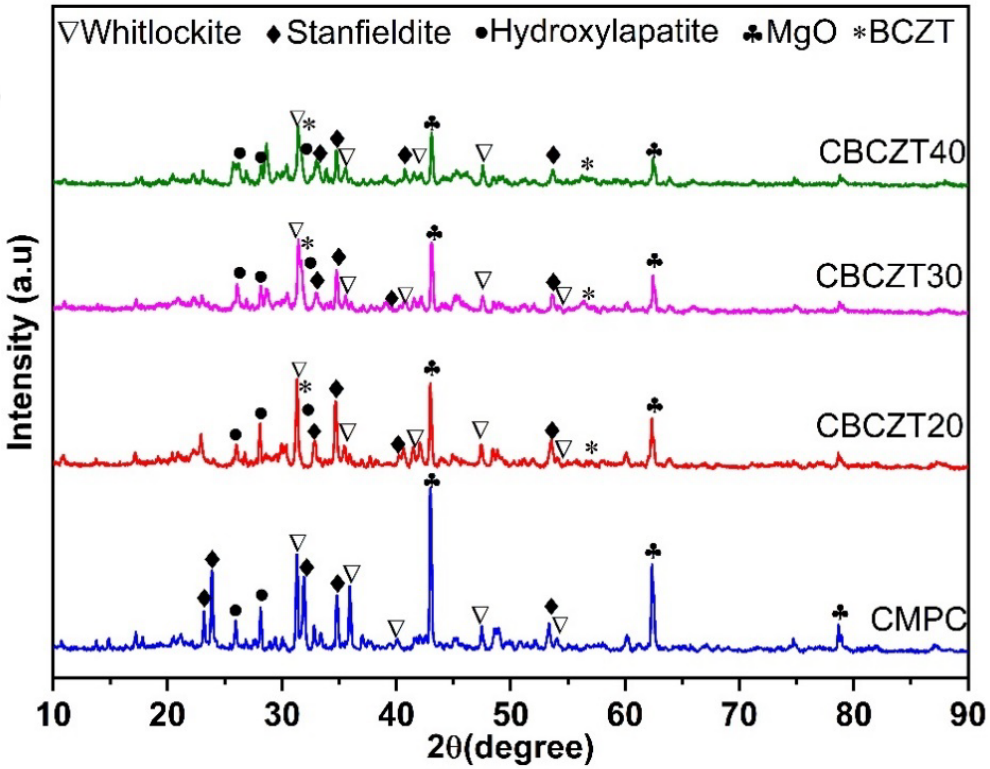


Figure 4.4 XRD patterns of the sintered composite ceramics

## 4.2 Morphologic Structure Analysis

Figure 4.5 shows the morphological structure of CMPC powder. It can be said that the particles are highly agglomerated and grouped into plate-shaped structures. CMPC occurs in multiphase structures with $CaHPO_4$ (DCPA), $Ca_4P_2O_9$ (TTCP), $(Ca_3PO_4)_2$ (TCP), and MgO. Therefore, different crystal shapes such as triangles and honeycombs are seen in the SEM images (represented by squares). It is hard to determine which crystal shape belongs to which phase. However, it is thought that the triangular shape can belong to DCPA or DCPD ($CaHPO_4.\ 2H_2O$) (Tas, 2016).

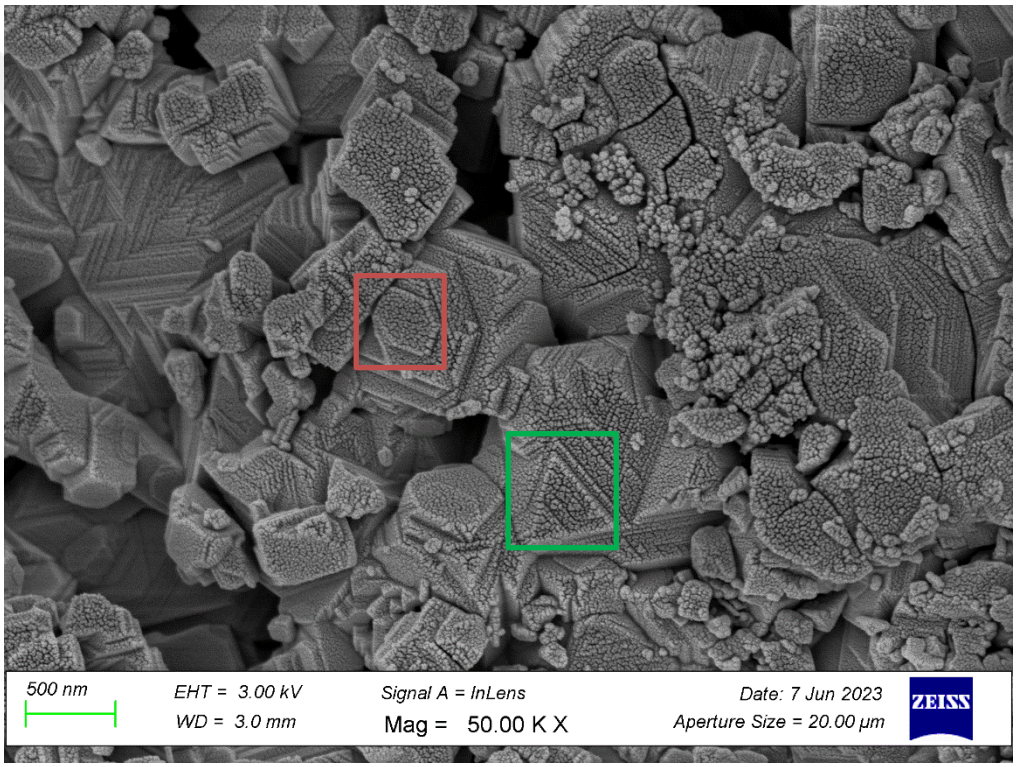


Figure 4.5 SEM images of CMPC

BCZT particles with different shapes and sizes are seen in Figure 4.6. The tetragonal and orthorhombic phases were excepted because of the obtained XRD results of BCZT. Also, it can be said that the particles were agglomerated. The size of the particles varied between 131.4 nm and 294.5 nm. Since BCZT was synthesized via the sol-gel method, the particles were obtained in small sizes.

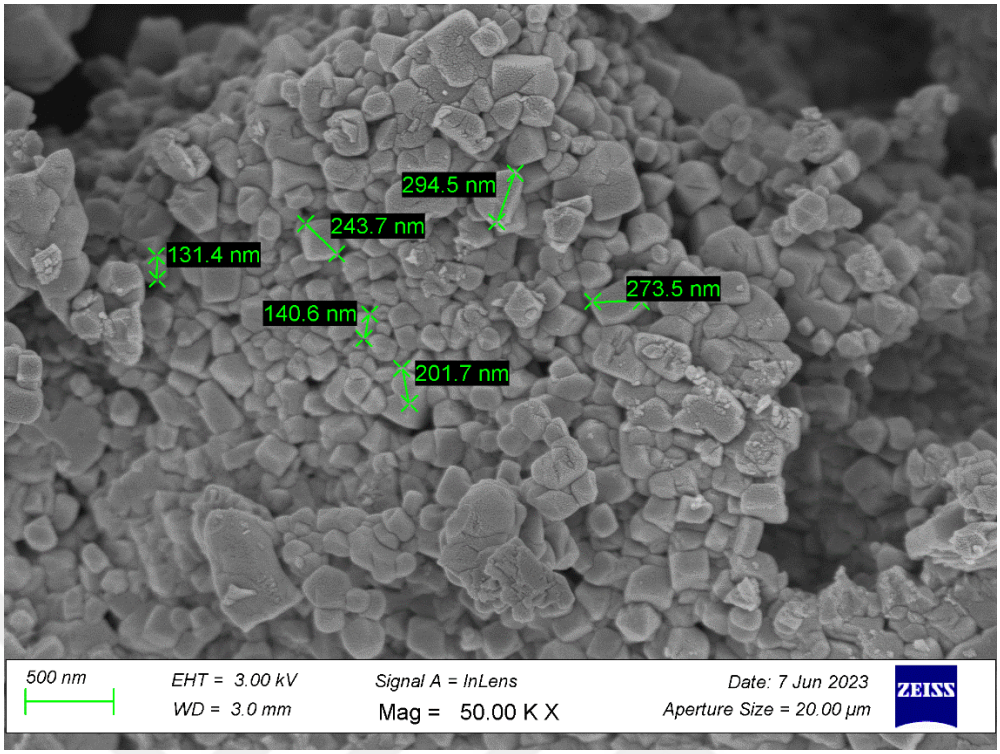


Figure 4.6 The morphological structure of BCZT

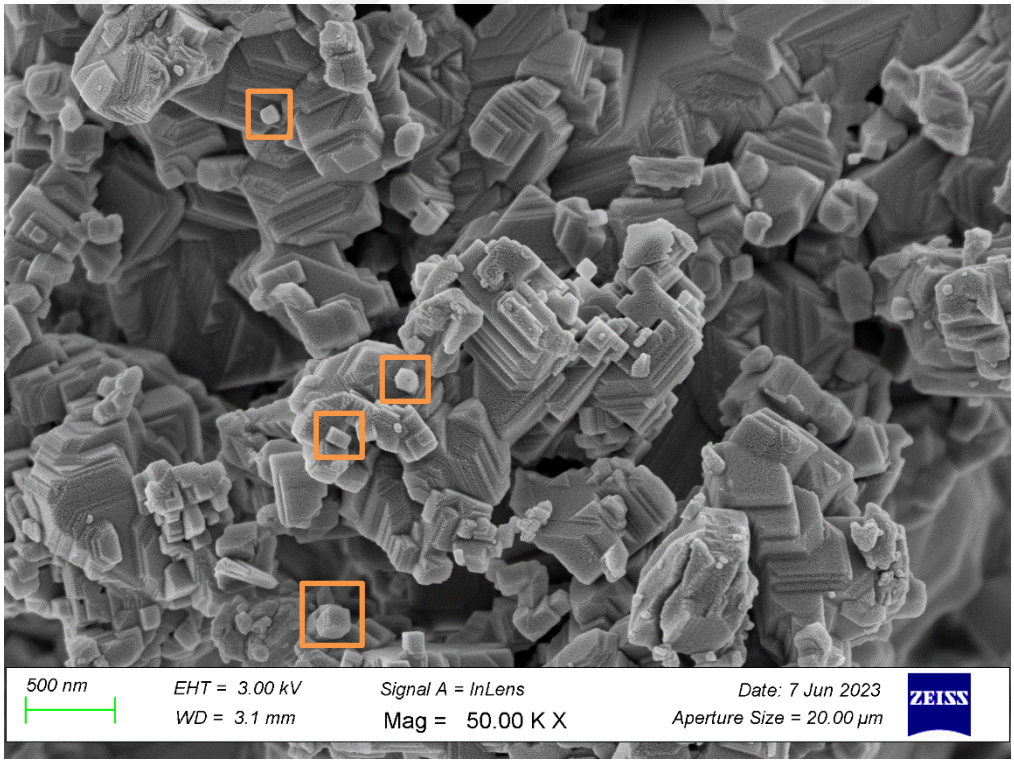


Figure 4.7 Scanning electron microscope images of CBCZT30

Figure 4.7 represents SEM images of CBCZT30 (with 30% of BCZT additive). The particles that are shown by squares look different than plate-like structures of CMPC. It is thought that the pointed particles probably belong to BCZT due to their smaller shapes and sizes.

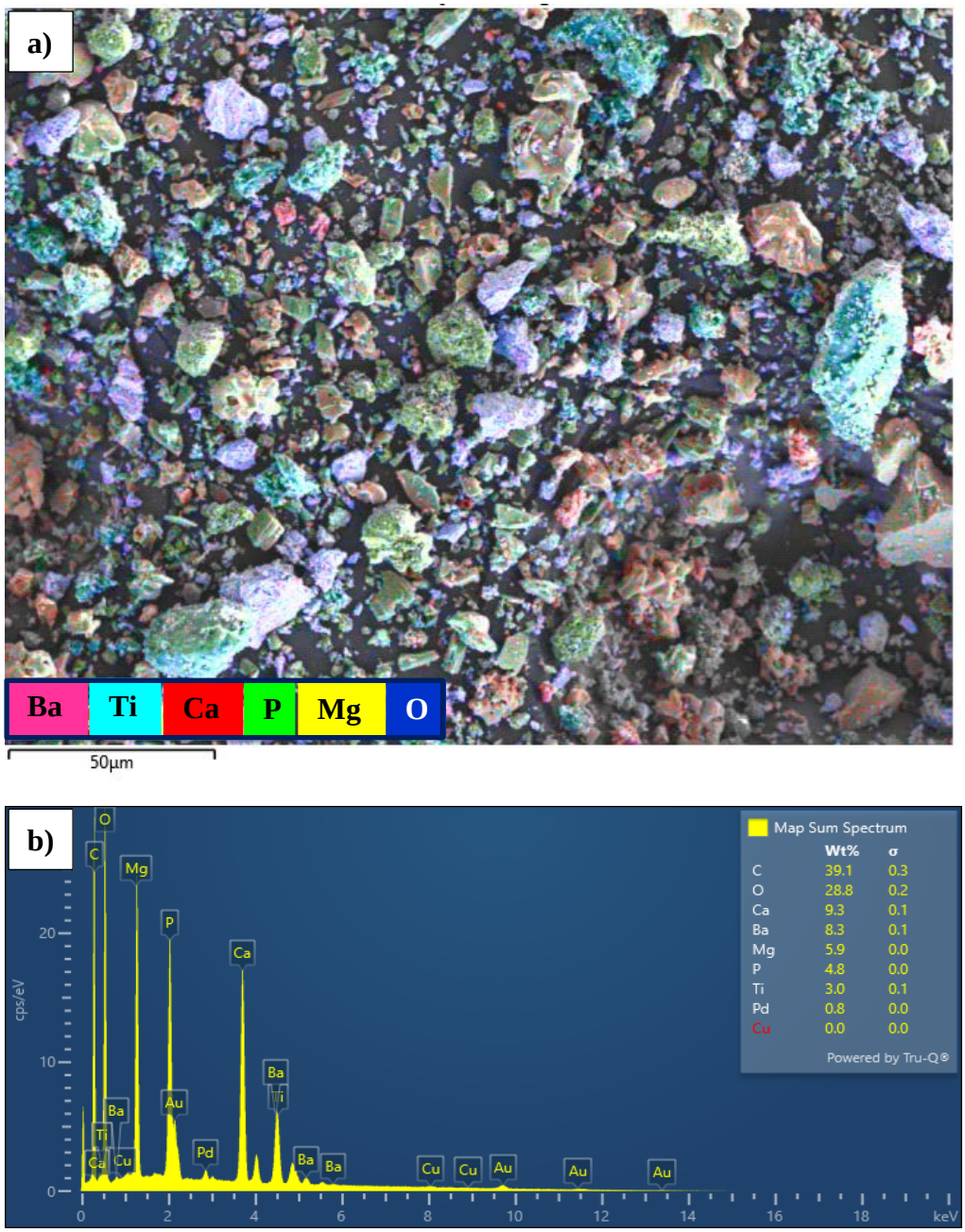


Figure 4.8 (a) SEM-EDS image of CBCZT30 in color-coded mapping (500 X magnification, 3.0 kV working voltage, and 3.0 mm working distance), (b) EDS spectrum of CBCZT30

Figure 4.8 (a) displays the color-coded elementel distribution of Ca, Mg, P, O, Ba, and Ti elements, and Figure 4.8 (b) shows the weight percentage of the elements in CBCZT30 from the image given in Figure 4.8 (a). Besides Figure 4.8, Figure 4.9 represents an elemental mapping of the related elements. Thus, it can be evaluated the homogenization of the contents in the composite sample.

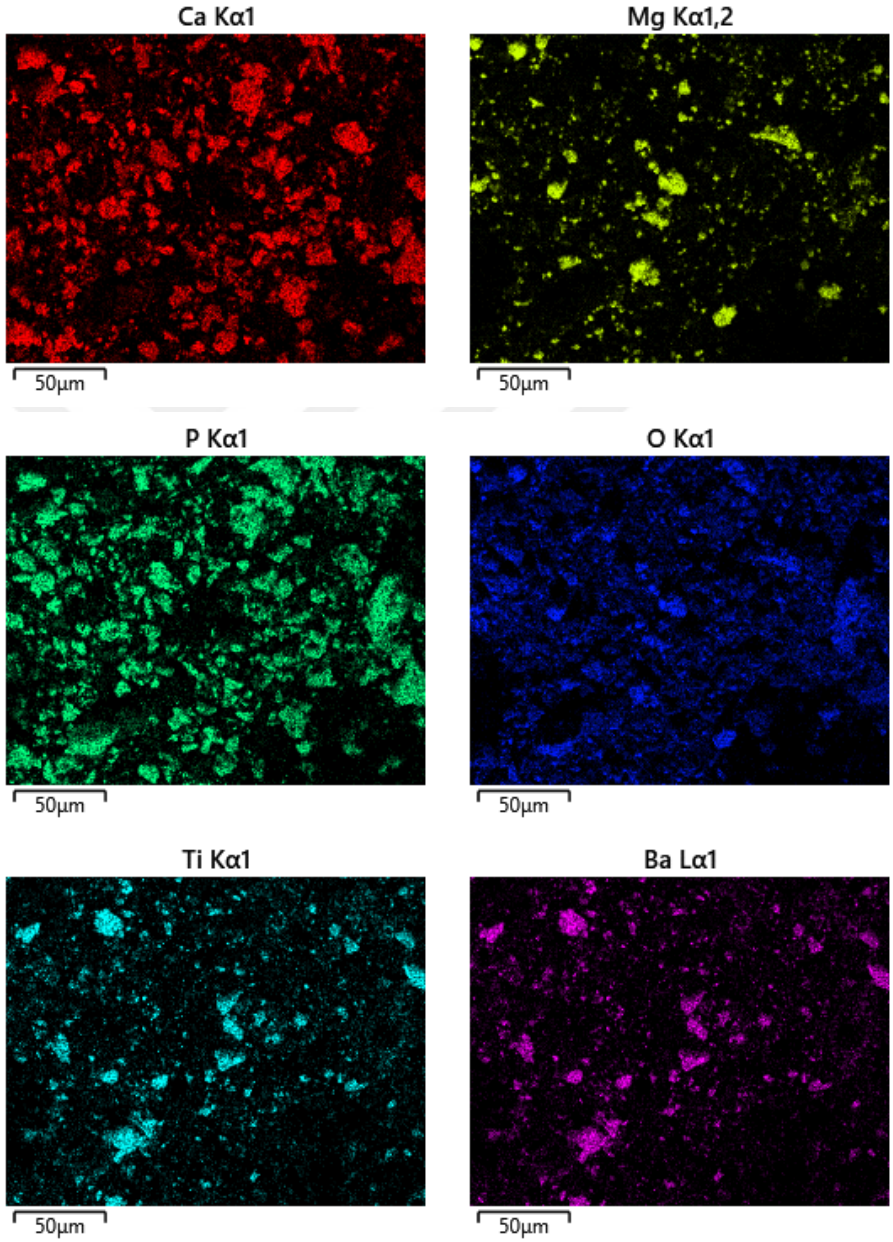


Figure 4.9 EDS mapping spectra of the related elements in CBCZT30

It can be said that in Figure 4.8 (a) and Figure 4.9 the presence of Ca, P, Mg elements are more than Ba and Ti elements, as expected. On the other hand, Figure 4.8 (b) gives some information about the weight percentage of the elements in related images of CBCZT30. Here, the elements Pd, Au, and C do not belong to the composition of the sample. They were used to provide the conductivity required for SEM analysis. The other intense peaks in the EDS analysis belonged to Ca, P, and Mg elements. O is one of the highest peaks after C. Because O is a common element of the possible phases such as MgO, $CaHPO_4$, $Ca_3(PO_4)_2$, $Ca_4P_2O_4$, and BCZT in the structure. Also, Ba and Ti peaks are the smallest over the peaks of Ca, Mg, and P, since they were used in less quantity (30 wt%) in the composite.

## 4.3 Particle Size Analysis

Figure 4.10 illustrates the particle size distribution curves for the BCZT, CPC, and MPC powders. MPC demonstrates a narrower particle size distribution, while CPC exhibits a coarse-side shoulder. In contrast, BCZT displays a bimodal distribution, likely due to the agglomeration of smaller particles. The agglomeration of the particles can be seen in Figure 4.6.

The particle size of the powders was measured to determine their span, median, and mean size values. Span is a parameter used to measure the width of the particle size distribution. A decrease in the span value results in a narrower particle size distribution, indicating a direct correlation between the span value and the width of the particle size distribution (Govoreanu et al., 2009; Kirby-Smith et al., 2023). BCZT, CPC, and MPC have span values of 3.402, 2.800, and 2.163, respectively. This indicates that particles in MPC have more similar sizes compared to those in BCZT and CPC. The median (d50) represents the middle value of the data set, indicating that half of the microparticles are smaller than this value (Türkoğlu et al., 2023). The median size of BCZT, CPC, and MPC were 15.060 µm, 17.820 µm, and 20.8622 µm, respectively. The mean values for MPC, CPC, and BCZT were 27.190 µm, 24.303 µm, and 24.048 µm, respectively.

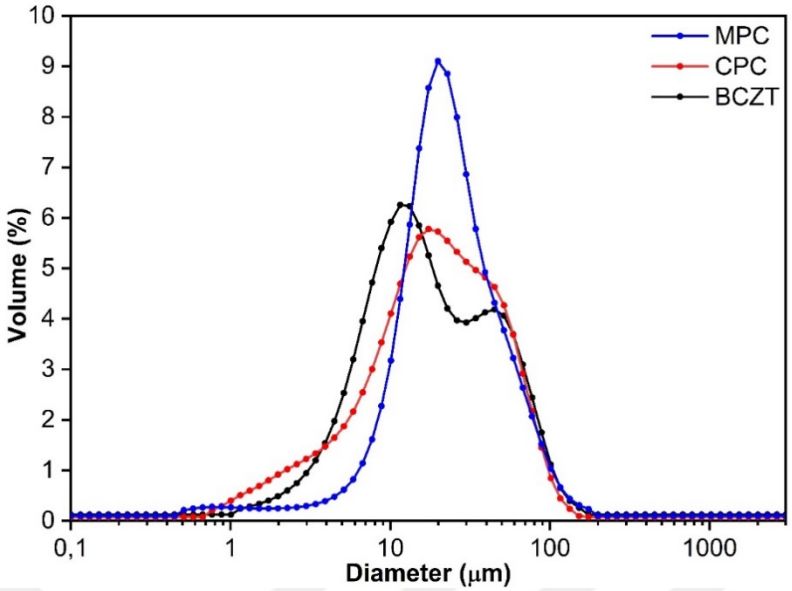


Figure 4.10 Size distribution histograms of BCZT, CPC, and MPC powders

## 4.4 Dielectric and piezoelectric behavior of the samples

Figure 4.11 shows the frequency-dependent dielectric constant (Ɛr) characteristics of the samples at room temperature. The ferroelectric hysteresis loop and corresponding electric-field induced strain curve in Figure 4.12 demonstrate the ferroelectric and piezoelectric characteristics of the BCZT sample in the morphotropic phase boundary region, along with a large dielectric constant. The $d_{33}$ value of this sample (263 pC/N) confirms its high piezoelectric nature, as shown in Table 4.2. CMPC shows low dielectric constant values within the range of 1-100 kHz, as anticipated. (Kaygili et al., 2016). Composite materials show increased dielectric constant with the increasing BCZT compositional ratio, particularly prominent at 100 kHz, where the dielectric constant reaches a plateau. The dielectric loss values were measured as 0.0217, 0.0016, 0.0061, 0.0207, and 0.0453 for BCZT, CMPC, CBCZT20, CBCZT30 and CBCZT40, respectively. As predicted, and in line with the increasing dielectric constant, the dielectric loss rises as the BCZT content does (see Table 4.2).

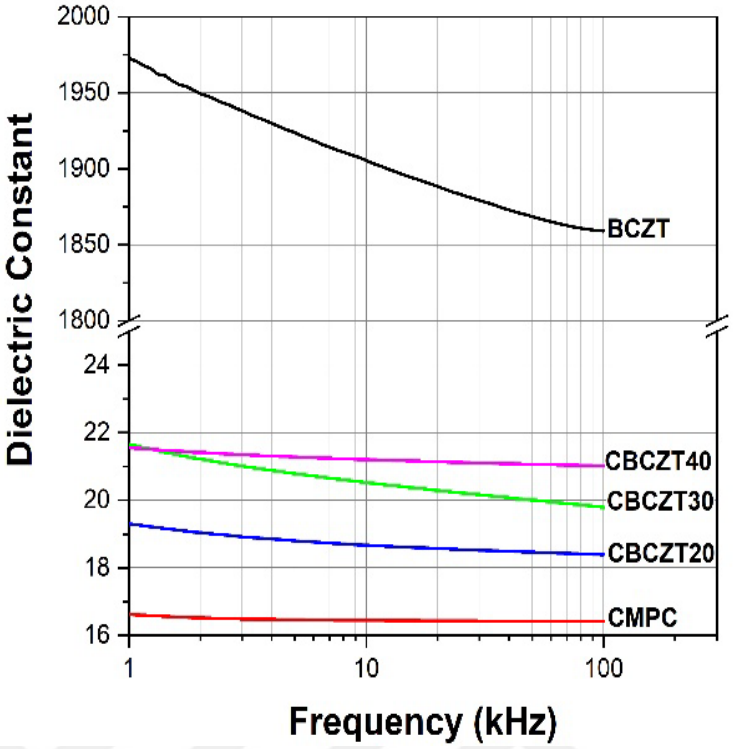


Figure 4.11 The frequency-dependent dielectric constant of all samples at RT

Table 4.2 The density, d33 coefficient, εr constant, and dielectric loss values of the composite ceramics

| Sample | Density ($g/mm^3$) | $d_{33}$ (pC/N) | $\varepsilon_r$ | Dielectric Loss Values |
|---|---|---|---|---|
| CMPC | 1.94 | - | 16.407 | 0.0016 |
| CBCZT20 | 2.09 | 1.9 | 18.386 | 0.0061 |
| CBCZT30 | 2.42 | 2.0 | 19.794 | 0.0207 |
| CBCZT40 | 2.60 | 2.3 | 21.018 | 0.0453 |

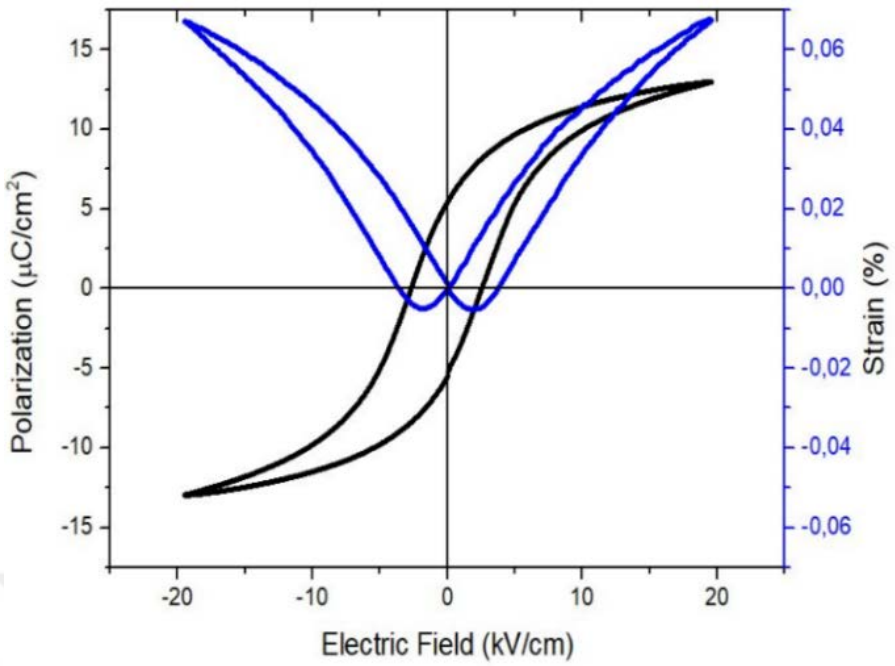


Figure 4.12 The hysteresis loop and electric field-induced strain curve of BCZT

Before measuring the $d_{33}$ coefficient, all samples underwent a poling process to enhance their piezoelectricity. This process involved aligning the ferroelectric domains of a polycrystalline ceramic using a strong electric field (Rotan et al., 2020). The poling process is mainly carried out in two ways: the contact (conventional) method and the corona method (non-contact). In the contact method, both the sample surfaces are electroded before polarization, for example, using a silver paste. The process is conducted in a dielectric medium (usually silicone oil) to prevent the formation of sparks. In the corona method, the sample does not need to be electroded before polarization. The polarization is performed in ionized air. Corona poling is a non-contact and biologically safer electrical poling technique compared to typical contact polarization methods. It does not require electrodes and insulating liquids. (Cholleti, 2018; Xu et al., 2024). Overall, non-contact poling offers several advantages over contact poling, especially in terms of preventing contamination, reducing damage, improving uniformity, and being compatible with sensitive materials. (Tansel et al., 2013).

A slight increase in the piezoelectric coefficient of the composites (i.e. d33) correlates with a small increase in the dielectric constant up to 20 as the BCZT

increases. Upon precise examination, it was observed that the $d_{33}$ coefficient experienced an increase within the range of 1.9 to 2.3 pC/N for composition ratios between 20% to 40% (see Table 4.2). It's important to note that the $d_{33}$ coefficient of corona-poled samples was not affected by whether they had a silver paste coating or not. A study by Rotan et al. in 2020 also found that, for the corona poling method, silver coating the samples before polarization did not affect were the efficiency of polarization. The study emphasized that the poling is better polarization without silver coating is important to avoid toxic effects when dealing with biomaterials (Rotan et al., 2020).

BCZT plays a crucial role as the piezoelectric constituted in the composites, demonstrating an impressive piezoelectric coefficient of 263 pC/N. By increasing the BCZT ratio, the $d_{33}$ coefficient of the composites is significantly enhanced, reaching a maximum of 2.3 pC/N for 40% of BCZT. In a related study in the literature, a similar content of piezoelectric additives was utilized, resulting in the achievement of a $d_{33}$ value of 2.53 pC/N with a 40% piezoelectric additive composition. (T. Wu et al., 2023). On the other hand, the piezoelectric performance of a ceramic material is influenced by its density. Ceramics with higher density are anticipated to demonstrate improved piezoelectric performance due to the lack of lower permittivity pores. (Poon et al., 2020). The measured density values for BCZT, CMPC, CBCZT20, CBCZT30, and CBCZT40 are 4.98, 1.94, 2.09, 2.42, and 2.60 $g/mm^3$, respectively. The relationship between the $d_{33}$ coefficient and the density of the samples with varying BCZT content is illustrated in Figure 4.13. Both the density and $d_{33}$ values increase as the BCZT content increases.

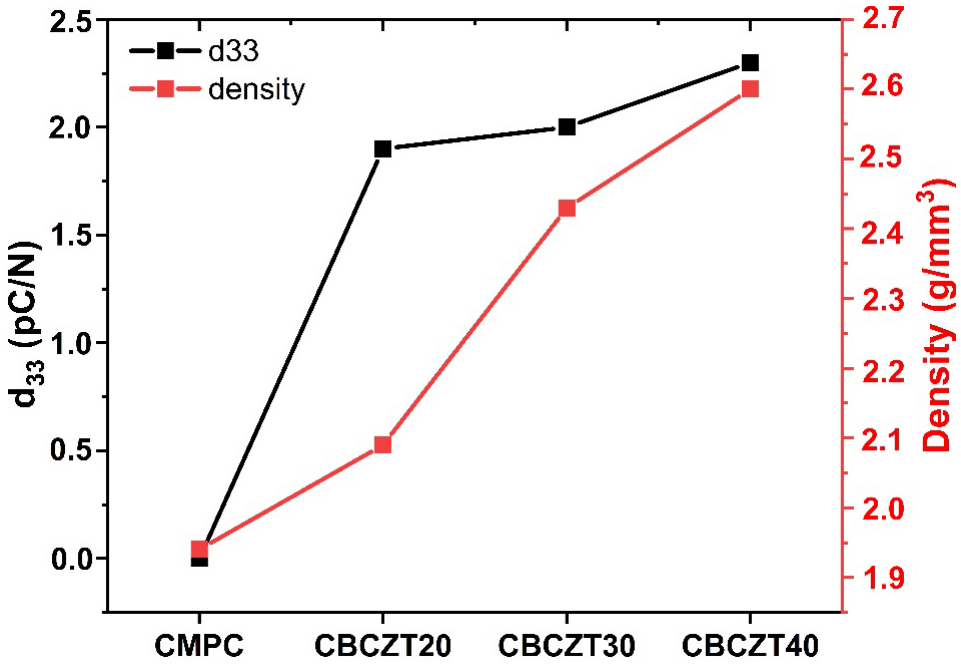


Figure 4.13 Variation graph of the d33 coefficient and density as a function of BCZT content

## 4.5 Injectability and Setting Time

It is essential for a cement paste to have good injectability and setting time, as these properties affect its performance in invasive surgeries. The setting kinetics of the cement paste are directly related to these two properties. Cement paste setting and hardening occur due to phase transformation based on precipitation and dissolution activities. When hydrophilic cement particles are mixed with water, a chemical reaction between the cement and water begins. This process, like what happens with Portland cement, causes the cement to harden and gain increased mechanical strength over time. Additionally, the chemical composition of the cement affects the chemical reactions during the setting process. In most cases, adding particles with no setting capability affects the setting process of the injectable bone scaffold, causing a delay in setting time but improving injectability. (T. Wu et al., 2023). In our study, the cement utilized in the composites comprised a 1:1 blend of CPC and MPC, and the piezoelectric additive incorporated in the composites was BCZT. The P/L ratio significantly influences injectability and the setting times (*ti* and *tf*). Elevated liquid content in the paste enhances injectability but compromises mechanical properties due to the development of micro-pores. On the flip side, reducing the water content below

the optimum level causes packing irregularities and detrimental effects on the workability and injectability of bone cement during surgery (Bohner & Baroud, 2005; Hofmann et al., 2009; Şahin & Kalyon, 2017). The injectability improved with increasing BCZT addition, as expected because the BCZT particles inhibit hydration reactions between the cement and water ions. The presence of BCZT particles slows down the relation between cement ions. Additionally, the good injectability of the prepared paste may be due to the particle size distribution. It is important to note that the compatibility of the particle size distribution of the components is crucial for injectability. The results of the particle size distribution (refer to Figure 4.10) indicate that the particles are in harmony with each other. In orthopedic surgery, the timing from the preparation to the injection of the paste into the damaged tissue plays a critical role and is directly linked to the initial setting time (*ti*) when the cement begins to lose its plasticity. It is essential for the injection of the paste to be completed before *ti*. Conversely, at *tf*, the cement achieves significant hardening and gains a specific structural strength. The wound closure is recommended after *tf*. According to the literature, the suggested *ti* is approximately 8 minutes, and *tf* is approximately 15 minutes (Jansen et al., 2005; F. Wu et al., 2008)

Table 4.3 The injectability percentage and setting time of the prepared bone cement composites

| Sample | Injectability (%) | Setting time (min) | |
|---|---|---|---|
| | | Initial (*ti*) | Final (*tf*) |
| CMPC | 78,32 | 5 | 14 |
| CBCZT20 | 84,99 | 7 | 17 |
| CBCZT30 | 85,12 | 9 | 18 |
| CBCZT40 | 86,16 | 11 | 32 |

When comparing the *ti* and *tf* values of the samples, it was found that CMPC had the lowest values at 4 minutes and 14 minutes, respectively. CBCZT20 and CBCZT30 exhibited similar *ti* and *tf* values, while CBCZT40 had a *ti* of 11 minutes and *tf* of 32 minutes. Despite the P/L ratio remaining unchanged, the increase in BCZT in the composites led to a delay in the hydration reactions of the cement. As a result, an

increasing BCZT ratio caused an increase in both *ti* and *tf* values (see Figure 4.14 and Table 4.3).

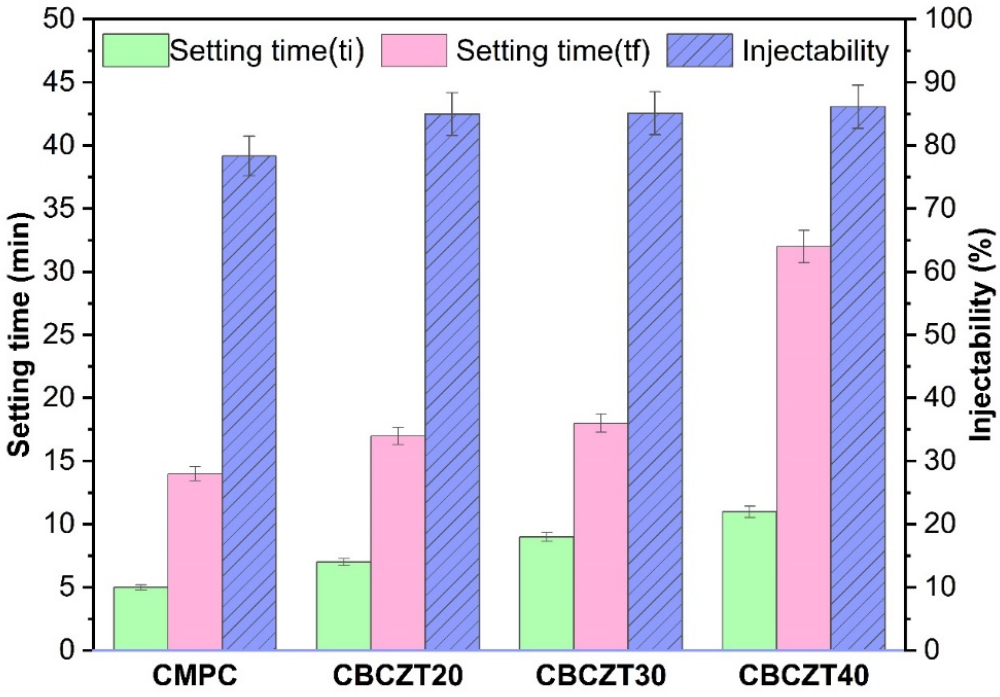


Figure 4.14 Injectability and setting time (***ti*** and ***tf***) of the cements at a fixed P/L ratio of 1.55 g/ml

## 4.6 Compressive Strength

Bone scaffolds are created to aid in the healing of damaged bone tissue. As a result, tissue scaffolds should mimic natural bone in many ways and be compatible with the mechanical properties of the area in which they are used. Bones in the human body have varying mechanical properties based on their structure and function, typically expressed in terms of compressive strength. The compressive strength values for different types of bones are as follows: human trabecular bone (30 MPa) (Jansen et al., 2005), cortical bone (90 to 209 MPa), and cancellous bone (1.5 to 45 MPa) (Ginebra, 2009).

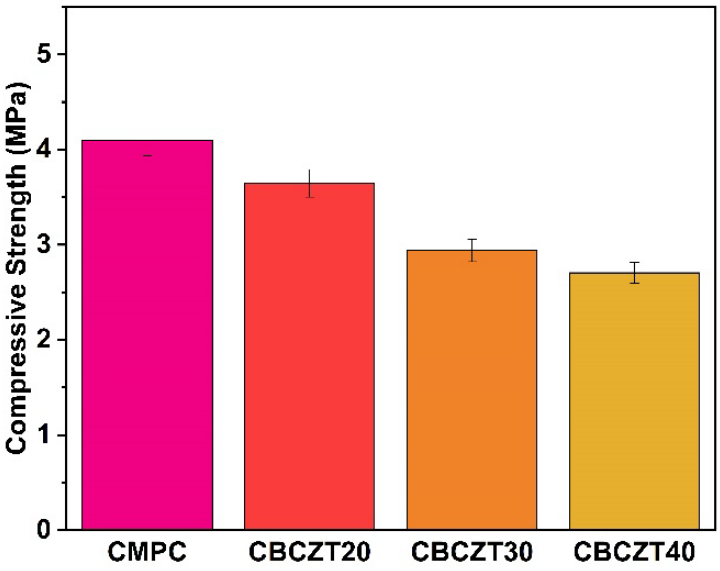


Figure 4.15 The compressive strength of the bone cements after 24 h

The compressive strength values for CMPC, CBCZT20, CBCZT30, and CBCZT40 after 24 hours of hydration are shown in Figure 4.15 and Table 4.4. CMPC exhibited the highest compressive strength at 4.109±0.54 MPa. The compressive strength of the composite samples decreased as the BCZT content increased. One possible explanation for this decrease is that the non-hydrating BCZT, when used in small amounts in the composites, may be surrounded by the hydrating CPC and MPC particles. However, it became more difficult to keep hydrated as the BCZT ratio increased. This led to a decrease in compressive strength and an increase in setting time.

Figure 4.16 shows compressive strengths over time for CMPC and CBCZT30. CMPC was used as the control sample, while CBCZT30 was chosen for its good injectability, suitable setting times (*ti* and *tf*), and relatively higher $d_{33}$ coefficient. The results indicated that the compressive strength of both CMPC and CBCZT30 samples improved as the reaction time increased. The addition of BCZT slowed down the increase in the compressive strength of CMPC. However, the compressive strength values of both CMPC and CBCZT30 samples are within the 1.5-45 MPa range, which is suitable for cancellous bone. Additionally, the BCZT addition improved the injectability of the CMPC cement.

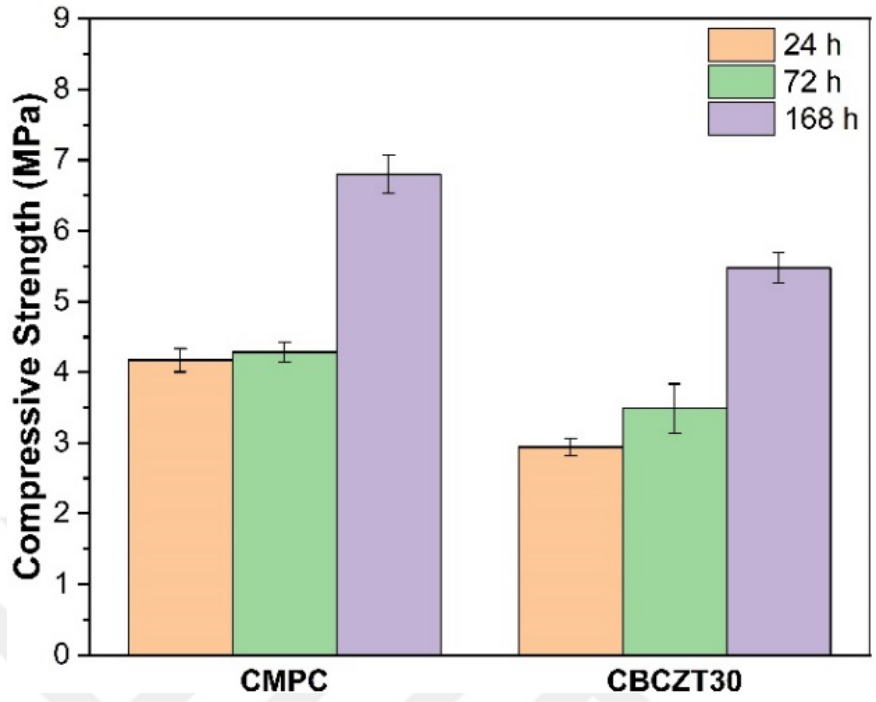


Figure 4.16 The compressive strength of CMPC and CBCZT30 after 24h, 72h, and 168h

Table 4.4 Characterization results of the samples

| Sample | Compressive Strength (MPa) | | |
|---|---|---|---|
| | 24h | 72h | 168h |
| CMPC | 4.109 ±0.54 | 4.284±0.13 | 6.801±0.51 |
| CBCZT20 | 3.645 ±0.47 | - | - |
| CBCZT30 | 2.940 ±0.65 | 3.484±0.35 | 5.477±0.39 |
| CBCZT40 | 2.705 ±0.37 | - | - |

The research assessed the changes in phase composition of CMPC cement with and without BCZT after being hydrated for 0h, 24h, 72h, and 168h using XRD analysis, as shown in Figure 4.17 and Figure 4.18. In these figures, it is noticeable that the anhydrated (0h) CMPC sample is dominated by TTCP (JCPDS:00-025-1137) and MgO (JCPDS: 00-045-0946) peaks. However, after 24 hours of hydration, small amounts of HA (JCPDS:01-072-1243) and struvite ($NH_4MgPO_4.6H_2O$, JCPDS:00-015-0762) phases appeared in the CMPC. The intensities of the HA and struvite peaks

continued to increase after 72 hours and 168 hours. This phase change is likely due to the conversion of TTCP to HA and MgO to struvite as a result of hydration (Burguera et al., 2006; F. Wu et al., 2008).

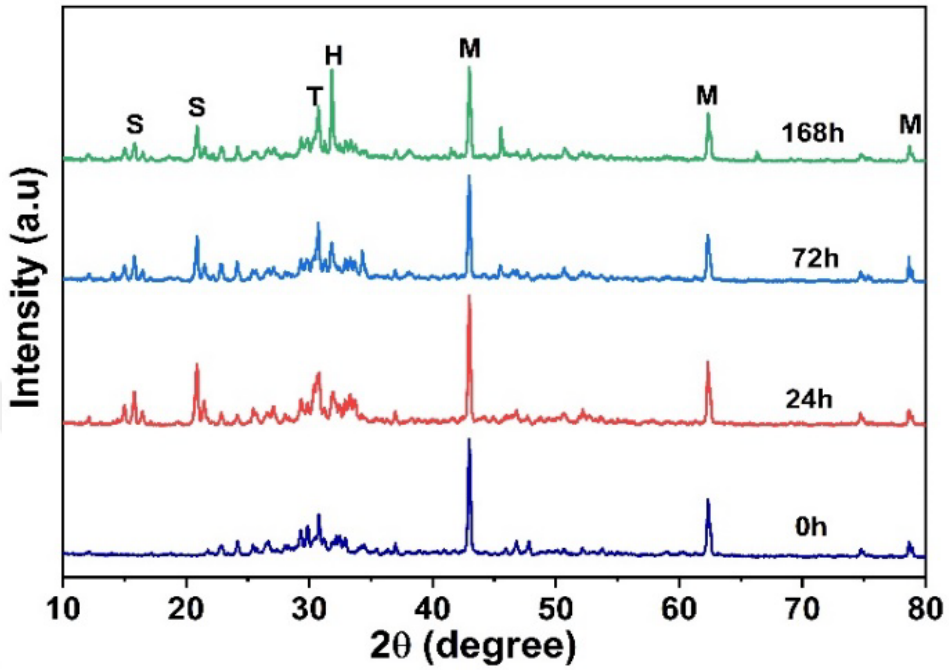


Figure 4.17 XRD pattern of CMPC after soaking Ringer solution for 0-168 h

Based on the X-ray diffraction (XRD) pattern, the peaks of the materials HA (JCPDS: 01-072-1243), and BCZT (JCPDS: 01-081-2198) were observed at 2θ 31.741° and 2θ 31.598°, respectively. These peaks likely overlapped with the highest peak at 2θ 31.651° in the XRD pattern. The consistent BCZT ratio in the composite material may have contributed to the slight increase in the intensity of the highest peak. This increase could be linked to the gradual formation of the HA phase during the soaking period.

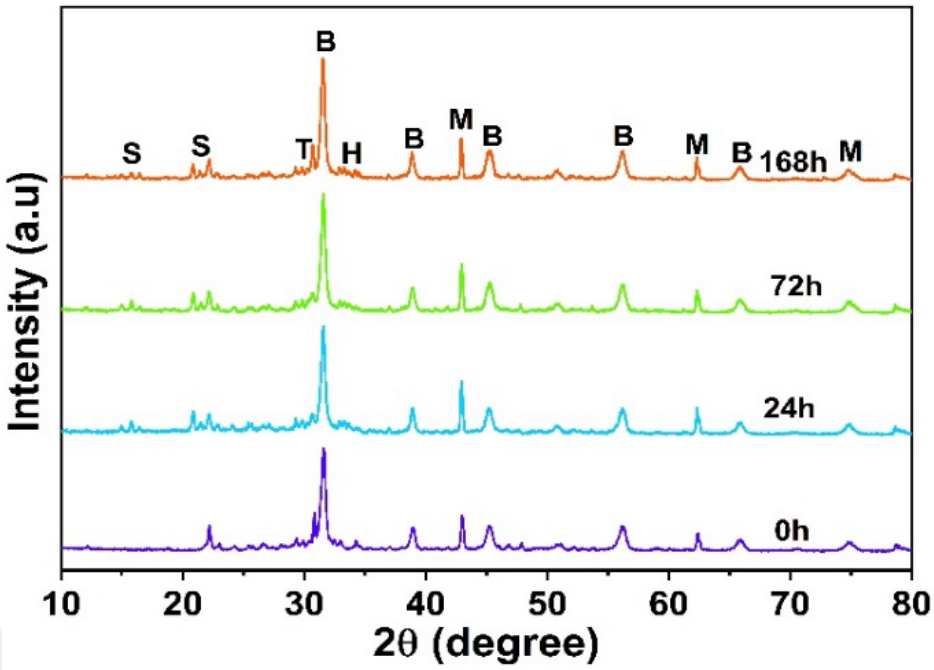


Figure 4.18 XRD pattern of CBCZT30 after soaking Ringer solution for 0-168 h

# CHAPTER FIVE
# CONCLUSION AND FUTURE WORK

The primary objective of this study is to introduce a new injectable composite bone cement composition consisting of piezoelectric BCZT and CPC-MPC bone cement. This composition holds potential for applications in bone tissue engineering. BCZT, synthesized through the sol-gel method, exhibits a ferroelectric property, containing tetragonal and orthorhombic crystal phases.

The morphological investigation shows that CMPC particles have plate-like structures. BCZT particles are smaller size with different shapes than CMPC particles. The elementel mapping and EDS analysis of the composite sample, CBCZT30, showed that BCZT particles were well distributed in CMPC.

The $d_{33}$ coefficient of BCZT was measured as 263 pC/N. Thus, the prepared composites with three different ratios of BCZT, namely CBCZT20, CBCZT30, and CBCZT40, showed piezoelectric properties with the $d_{33}$ coefficients of 1.9 pC/N, 2.0 pC/N, and 2.3 pC/N, respectively.

All the composite cement prepared at a constant P/L ratio of 1.55 g/ml showed good injectability over 70%, which is required in invasive surgery, and this property was enhanced with increasing BCZT ratios. However, BCZT addition delayed the setting reaction, and therefore setting times gradually increased. In addition, compressive strength values decreased upon increasing BCZT, but they were within the 1.5-45 MPa range which is sufficient for cancellous bone.

When the results of injectability, setting time, and mechanical strength of all the composite samples were considered, CBCZT30 was evaluated as the optimum injectable composite bone cement composition. It also exhibited a piezoelectric coefficient higher than that of natural bone which is 0.7 pC/N. Consequently, this novel bone cement composition is found to be promising in bone healing applications by invasive surgery.

For future works, the mineralization tendencies of the produced piezoelectric bone cements will be investigated. In addition, their biocompatibility will be analyzed by performing cytotoxicity and cell viability tests on bone marrow-derived mesenchymal stem cells under in vitro conditions. In addition, it will be investigated whether it will accelerate the healing of damaged tissue by applying static and dynamic loads in vitro.

## REFERENCES


Acosta, M., Detsch, R., Grünewald, A., Rojas, V., Schultheiß, J., Wajda, A., Stark, R. W., Narayan, S., Sitarz, M., Koruza, J., & Boccaccini, A. R. (2018). Cytotoxicity, chemical stability, and surface properties of ferroelectric ceramics for biomaterials. *Journal of the American Ceramic Society*, *101*(1), 440–449. https://doi.org/10.1111/jace.15193

Adamiak, K., & Atten, P. (2004). Simulation of corona discharge in point–plane configuration. *Journal of Electrostatics*, *61*(2), 85–98.

Al-Tabbaa, A. (2013). Reactive magnesia cement. *Eco-Efficient Concrete*, 523–543. https://doi.org/10.1533/9780857098993.4.523

Ambard, A. J., & Mueninghoff, L. (2006). Calcium phosphate cement: review of mechanical and biological properties. *Journal of Prosthodontics*, *15*(5), 321–328.

Arjunan, A., Baroutaji, A., Praveen, A. S., Robinson, J., & Wang, C. (2020). *Classification of biomaterial functionality*.

Barba, A., Maazouz, Y., Diez-Escudero, A., Rappe, K., Espanol, M., Montufar, E. B., Öhman-Mägi, C., Persson, C., Fontecha, P., Manzanares, M. C., Franch, J., & Ginebra, M. P. (2018). Osteogenesis by foamed and 3D-printed nanostructured calcium phosphate scaffolds: Effect of pore architecture. *Acta Biomaterialia*, *79*, 135–147. https://doi.org/10.1016/j.actbio.2018.09.003

Bechmann, R. (1956). Elastic, piezoelectric, and dielectric constants of polarized barium titanate ceramics and some applications of the piezoelectric equations. *The Journal of the Acoustical Society of America*, *28*(3), 347–350.

Behera, A. (2021). *Advanced materials: an introduction to modern materials science*. Springer Nature.

Bharadwaj, A. (2021). An overview on biomaterials and its applications in medical science. *IOP Conference Series: Materials Science and Engineering*, *1116*(1), 12178.

Bhat, S., & Kumar, A. (2013). Biomaterials and bioengineering tomorrow's healthcare. *Biomatter*, *3*(3). https://doi.org/10.4161/biom.24717

Bijalwan, V., Sokolov, I., & Tofel, P. (2021). Poling procedures and piezoelectric response of (Ba0. 85Ca0. 15Zr0. 1T0. 9) O3 ceramics. *Journal of Asian Ceramic Societies*, *9*(1), 229–236.

Birchal, V. S. S., Rocha, S. D. F., & Ciminelli, V. S. T. (2000). The effect of magnesite calcination conditions on magnesia hydration. *Minerals Engineering*, *13*(14–15), 1629–1633.

Bocanegra-Bernal, M. H. (2008). Microstructural evolution during sintering in MgO powders precipitated from sea water under induced agglomeration conditions. *Powder Technology*, *186*(3), 267–272.

Bohner, M. (2008). Bioresorbable ceramics. *Degradation Rate of Bioresorbable Materials*, 95–114.

Bohner, M., & Baroud, G. (2005). Injectability of calcium phosphate pastes. *Biomaterials*, *26*(13), 1553–1563.

Bur, A. J. (1976). Measurements of the dynamic piezoelectric properties of bone as a function of temperature and humidity. *Journal of Biomechanics*, *9*(8), 495–507. https://doi.org/10.1016/0021-9290(76)90066-X

Burguera, E. F., Xu, H. H. K., & Weir, M. D. (2006). Injectable and rapid-setting calcium phosphate bone cement with dicalcium phosphate dihydrate. *Journal of Biomedical Materials Research - Part B Applied Biomaterials*, *77*(1), 126–134. https://doi.org/10.1002/jbm.b.30403

Chandrakala, E., Paul Praveen, J., Hazra, B. K., & Das, D. (2016). Effect of sintering temperature on structural, dielectric, piezoelectric and ferroelectric properties of sol-gel derived BZT-BCT ceramics. *Ceramics International*, *42*(4), 4964–4977. https://doi.org/10.1016/j.ceramint.2015.12.009

Chen, F., Song, Z., & Liu, C. (2015). Fast setting and anti-washout injectable calcium-magnesium phosphate cement for minimally invasive treatment of bone defects.

*Journal of Materials Chemistry B*, *3*(47), 9173–9181. https://doi.org/10.1039/c5tb01453k

Chen, X., Fan, H., Deng, X., Wu, L., Yi, T., Gu, L., Zhou, C., Fan, Y., & Zhang, X. (2018). Scaffold structural microenvironmental cues to guide tissue regeneration in bone tissue applications. *Nanomaterials*, *8*(11), 1–15. https://doi.org/10.3390/nano8110960

Cholleti, E. R. (2018). A Review on 3D printing of piezoelectric materials. *IOP Conference Series: Materials Science and Engineering*, *455*(1). https://doi.org/10.1088/1757-899X/455/1/012046

Dubey, A. K., & Kakimoto, K. I. (2016). Impedance spectroscopy and mechanical response of porous nanophase hydroxyapatite-barium titanate composite. *Materials Science and Engineering C*, *63*, 211–221. https://doi.org/10.1016/j.msec.2016.02.027

Faour, O., Dimitriou, R., Cousins, C. A., & Giannoudis, P. V. (2011). The use of bone graft substitutes in large cancellous voids: any specific needs? *Injury*, *42*, S87–S90.

Fernandez de Grado, G., Keller, L., Idoux-Gillet, Y., Wagner, Q., Musset, A.-M., Benkirane-Jessel, N., Bornert, F., & Offner, D. (2018). Bone substitutes: a review of their characteristics, clinical use, and perspectives for large bone defects management. *Journal of Tissue Engineering*, *9*, 2041731418776819.

Fu, D., & Itoh, M. (2015). Role of Ca off-centering in tuning ferroelectric phase transitions in Ba (Zr, Ti) O3 system. *Ferroelectric Materials—Synthesis and Characterization*.

Fukada, E., & Yasuda, I. (1957). On the Piezoelectric Effect of Bone. *Journal of the Physical Society of Japan*, *12*(10), 1158–1162. https://doi.org/10.1143/JPSJ.12.1158

Ginebra, M. P. (2009). Cements as bone repair materials. In *Bone Repair Biomaterials*. https://doi.org/10.1533/9781845696610.2.271

Govoreanu, R., Saveyn, H., Van der Meeren, P., Nopens, I., & Vanrolleghem, P. A. (2009). A methodological approach for direct quantification of the activated sludge floc size distribution by using different techniques. *Water Science and Technology*, *60*(7), 1857–1867.

Gutierrez Cisneros, C., Bloemen, V., & Mignon, A. (2021). Synthetic, natural, and semisynthetic polymer carriers for controlled nitric oxide release in dermal applications: a review. *Polymers*, *13*(5), 760.

Hermawan, H., Ramdan, D., & Djuansjah, J. R. P. (2011). Metals for biomedical applications. *Biomedical Engineering-from Theory to Applications*, *1*, 411–430.

Hofmann, M. P., Mohammed, A. R., Perrie, Y., Gbureck, U., & Barralet, J. E. (2009). High-strength resorbable brushite bone cement with controlled drug-releasing capabilities. *Acta Biomaterialia*, *5*(1), 43–49. https://doi.org/10.1016/j.actbio.2008.08.005

Ishikawa, K. (2014). Calcium phosphate cement. *Advances in Calcium Phosphate Biomaterials*, 199–227.

Jansen, J., Ooms, E., Verdonschot, N., & Wolke, J. (2005). Injectable calcium phosphate cement for bone repair and implant fixation. *Orthopedic Clinics of North America*, *36*(1), 89–95. https://doi.org/10.1016/j.ocl.2004.06.014

Jeong, J., Kim, J. H., Shim, J. H., Hwang, N. S., & Heo, C. Y. (2019). Bioactive calcium phosphate materials and applications in bone regeneration. *Biomaterials Research*, *23*(1), 1–11. https://doi.org/10.1186/s40824-018-0149-3

Jiann Chong, E. T., Ng, J. W., & Lee, P.-C. (2023). Classification and Medical Applications of Biomaterials–A Mini Review. *BIO Integration*.

Kalirajan, C., Dukle, A., Nathanael, A. J., Oh, T.-H., & Manivasagam, G. (2021). A critical review on polymeric biomaterials for biomedical applications. *Polymers*, *13*(17), 3015.

Kamel, T. M. (2007). *Poling and switching of PZT ceramics: field and grain size effects*.

Kapat, K., Shubhra, Q. T. H., Zhou, M., & Leeuwenburgh, S. (2020). Piezoelectric Nano-Biomaterials for Biomedicine and Tissue Regeneration. *Advanced Functional Materials*, *30*(44). https://doi.org/10.1002/adfm.201909045

Karabay, U., Husemoglu, R. B., Yüksel, M., & Havitcioglu, H. (2019). 3D Printed Polylactic Acid Scaffold For Dermal Tissue Engineering Application : The Fibroblast Proliferation in. *Jomit*, *1*(2), 51–56.

Kaygili, O., Keser, S., Ates, T., Kirbag, S., & Yakuphanoglu, F. (2016). Dielectric properties of calcium phosphate ceramics. *Medziagotyra*, *22*(1), 65–69. https://doi.org/10.5755/j01.ms.22.1.7222

Khan, M. I., & Upadhyay, T. C. (2021). General introduction to ferroelectrics. *Multifunctional Ferroelectric Materials*, 1–23.

Khare, D., Basu, B., & Dubey, A. K. (2020). Electrical stimulation and piezoelectric biomaterials for bone tissue engineering applications. *Biomaterials*, *258*, 120280. https://doi.org/10.1016/j.biomaterials.2020.120280

Kim, S. Y., & Jeon, S. H. (2012). Setting properties, mechanical strength and in vivo evaluation of calcium phosphate-based bone cements. *Journal of Industrial and Engineering Chemistry*, *18*(1), 128–136. https://doi.org/10.1016/j.jiec.2011.11.001

Kirby-Smith, C., Steenekamp, J., Steyn, D., Haasbroek-Pheiffer, A., Hamman, H., & Hamman, J. (2023). Intranasal Insulin Delivery: Microparticle Formulations Consisting of Aloe vera Polysaccharides for Advanced Delivery across Excised Olfactory and Respiratory Nasal Epithelial Tissues. *Applied Sciences*, *13*(8), 4822.

Kulinets, I. (2015). Biomaterials and their applications in medicine. In *Regulatory affairs for biomaterials and medical devices* (pp. 1–10). Elsevier.

Lang, S. B. (2016). Review of ferroelectric hydroxyapatite and its application to biomedicine*. *Phase Transitions*, *89*(7–8), 678–694. https://doi.org/10.1080/01411594.2016.1182166

Li, J.-F. (2021). *Lead-free piezoelectric materials*. John Wiley & Sons. https://doi.org/10.1002/9783527817047

Li, W., Xu, Z., Chu, R., Fu, P., & Zang, G. (2012). Structural and dielectric properties in the (Ba1− xCax)(Ti0. 95Zr0. 05) O3 ceramics. *Current Applied Physics*, *12*(3), 748–751.

Liu, W., & Ren, X. (2009). Large piezoelectric effect in Pb-free ceramics. *Physical Review Letters*, *103*(25), 1–4. https://doi.org/10.1103/PhysRevLett.103.257602

Liu, Z., Wu, H., Ren, W., & Ye, Z.-G. (2023). *Piezoelectric and ferroelectric materials: Fundamentals, recent progress, and applications*.

Manohar, C. S., Kumar, B. S., Sadhu, S. P. P., Srimadh, S. K., Muthukumar, V. S., Venketesh, S., & Varma, K. B. R. (2019). Novel Lead-free biocompatible piezoelectric hydroxyapatite (HA)–BCZT (Ba0. 85Ca0. 15Zr0. 1Ti0. 9O3) nanocrystal composites for bone regeneration. *Nanotechnology Reviews*, *8*(1), 61–78.

Montufar, E. B., Maazouz, Y., & Ginebra, M. P. (2013). Relevance of the setting reaction to the injectability of tricalcium phosphate pastes. *Acta Biomaterialia*, *9*(4), 6188–6198. https://doi.org/10.1016/j.actbio.2012.11.028

Park, S., Lee, C. W., Kang, M. G., Kim, S., Kim, H. J., Kwon, J. E., Park, S. Y., Kang, C. Y., Hong, K. S., & Nam, K. T. (2014). A ferroelectric photocatalyst for enhancing hydrogen evolution: Polarized particulate suspension. *Physical Chemistry Chemical Physics*, *16*(22), 10408–10413. https://doi.org/10.1039/c4cp01267d

Patra, A., Pal, A., & Sen, S. (2018). Polyvinylpyrrolidone modified barium zirconate titanate /polyvinylidene fluoride nanocomposites as self-powered sensor. *Ceramics International*, *44*(10), 11196–11203. https://doi.org/10.1016/j.ceramint.2018.03.150

Paul, S. (2019). *Biomedical engineering and its applications in healthcare* (S. Paul (ed.)). Springer. https://doi.org/10.1007/978-981-13-3705-5

Poon, K. K., Wurm, M. C., Evans, D. M., Einarsrud, M. A., Lutz, R., & Glaum, J. (2020). Biocompatibility of (Ba,Ca)(Zr,Ti)O3 piezoelectric ceramics for bone replacement materials. *Journal of Biomedical Materials Research - Part B Applied Biomaterials*, *108*(4), 1295–1303. https://doi.org/10.1002/jbm.b.34477

Praveen, J. P., Karthik, T., James, A. R., Chandrakala, E., Asthana, S., & Das, D. (2015). Effect of poling process on piezoelectric properties of sol-gel derived BZT-BCT ceramics. *Journal of the European Ceramic Society*, *35*(6), 1785–1798. https://doi.org/10.1016/j.jeurceramsoc.2014.12.010

Praveen, J. P., Kumar, K., James, A. R., Karthik, T., Asthana, S., & Das, D. (2014). Large piezoelectric strain observed in sol-gel derived BZT-BCT ceramics. *Current Applied Physics*, *14*(3), 396–402. https://doi.org/10.1016/j.cap.2013.12.026

Puli, V. S., Pradhan, D. K., Riggs, B. C., Adireddy, S., Katiyar, R. S., & Chrisey, D. B. (2014). Synthesis and characterization of lead-free ternary component BST–BCT–BZT ceramic capacitors. *Journal of Advanced Dielectrics*, *04*(02), 1450014. https://doi.org/10.1142/s2010135x14500143

Qiao, F., Chau, C. K., & Li, Z. (2009). Setting and strength development of magnesium phosphate cement paste. *Advances in Cement Research*, *21*(4), 175–180. https://doi.org/10.1680/adcr.9.00003

Qifeng, L., Jingjun, M., Sharma, M., & Vaish, R. (2019). Photocatalytic, piezocatalytic, and piezo-photocatalytic effects in ferroelectric (Ba0. 875Ca0. 125)(Ti0. 95Sn0. 05) O3 ceramics. *Journal of the American Ceramic Society*, *102*(10), 5807–5817.

Raj, N. P. M. J., Alluri, N. R., Khandelwal, G., & Kim, S.-J. (2021a). Ferroelectric flexible composite films based on morphotropic phase boundary for self-powered multisensors. *Chemical Engineering Journal*, *414*, 128840.

Raj, N. P. M. J., Alluri, N. R., Khandelwal, G., & Kim, S.-J. (2021b). The morphotropic phase boundary based BCST ferroelectric system for water remediation through Bi-catalytic activity. *Journal of Alloys and Compounds*, *871*,

159503.

Rotan, M., Zhuk, M., & Glaum, J. (2020). Activation of ferroelectric implant ceramics by corona discharge poling. *Journal of the European Ceramic Society*, *40*(15), 5402–5409.

Şahin, E., & Kalyon, D. M. (2017). The rheological behavior of a fast-setting calcium phosphate bone cement and its dependence on deformation conditions. *Journal of the Mechanical Behavior of Biomedical Materials*, *72*(May), 252–260. https://doi.org/10.1016/j.jmbbm.2017.05.017

Sakar, N., Ziylan Albayrak, A., Karakaya, M., Adem, U., & Tansel, T. (2024). Novel injectable calcium-magnesium phosphate cement-based composites with piezoelectric properties: advancements in bone regeneration applications. *Journal of Materials Science: Materials in Electronics*, *35*(15), 1–12. https://doi.org/10.1007/s10854-024-12761-8

Shand, M. A. (2006). *The chemistry and technology of magnesia*. John Wiley & Sons.

Sharma, M., Singhal, T., & Vaish, R. (2022). Effect of ferroelectric polarization on piezo/photocatalysis in Ag nanoparticles loaded 0.5 (Ba0. 7Ca0. 3) TiO3–0.5 Ba (Zr0. 1Ti0. 9) O3 composites towards the degradation of organic pollutants. *Journal of the American Ceramic Society*, *105*(5), 3165–3176.

Soudée, E., & Péra, J. (2000). Mechanism of setting reaction in magnesia-phosphate cements. *Cement and Concrete Research*, *30*(2), 315–321. https://doi.org/10.1016/S0008-8846(99)00254-9

Soudée, E., & Péra, J. (2002). Influence of magnesia surface on the setting time of magnesia-phosphate cement. *Cement and Concrete Research*, *32*(1), 153–157. https://doi.org/10.1016/S0008-8846(01)00647-0

Tang, Y., Wu, C., Zhang, P., Zhao, K., & Wu, Z. (2020). Degradation behaviour of non-sintered graphene/barium titanate/magnesium phosphate cement bio-piezoelectric composites. *Ceramics International*, *46*(8), 12626–12636. https://doi.org/10.1016/j.ceramint.2020.02.028

Tansel, T., Ener Rusen, S., & Rusen, A. (2013). Uniform, large surface-area polarization by modifying corona-electrodes geometry. *Review of Scientific Instruments*, *84*(1).

Tariq, U., Hussain, R., Tufail, K., Haider, Z., Tariq, R., & Ali, J. (2019). Injectable dicalcium phosphate bone cement prepared from biphasic calcium phosphate extracted from lamb bone. *Materials Science and Engineering: C*, *103*, 109863.

Tariverdian, T., Behnamghader, A., Brouki Milan, P., Barzegar-Bafrooei, H., & Mozafari, M. (2019). 3D-printed barium strontium titanate-based piezoelectric scaffolds for bone tissue engineering. *Ceramics International*, *45*(11), 14029–14038. https://doi.org/10.1016/j.ceramint.2019.04.102

Tas, A. C. (2016). Transformation of Brushite (CaHPO4· 2H2O) to Whitlockite (Ca9Mg (HPO4)(PO4) 6) or other CaPs in physiologically relevant solutions. *Journal of the American Ceramic Society*, *99*(4), 1200–1206. https://doi.org/10.1111/jace.14069

Tavangar, M., Heidari, F., Hayati, R., Tabatabaei, F., Vashaee, D., & Tayebi, L. (2020). Manufacturing and characterization of mechanical, biological and dielectric properties of hydroxyapatite-barium titanate nanocomposite scaffolds. *Ceramics International*, *46*(7), 9086–9095. https://doi.org/10.1016/j.ceramint.2019.12.157

Thomas, D., Gaspar, D., Sorushanova, A., Milcovich, G., Spanoudes, K., Mullen, A. M., O'Brien, T., Pandit, A., & Zeugolis, D. I. (2016). Scaffold and scaffold-free self-assembled systems in regenerative medicine. *Biotechnology and Bioengineering*, *113*(6), 1155–1163. https://doi.org/10.1002/bit.25869

Türk, S., Findik, F., & Özacar, M. (2023). Nanobiomaterials: Classifications and Properties. In *Handbook of Nanobioelectrochemistry: Application in Devices and Biomolecular Sensing* (pp. 19–42). Springer.

Türkoğlu, G. C., Erkan, G., Karavana, S. Y., Sarıışık, A. M., Çetmeli Bakadur, A., Ütebay, B., & Popescu, A. (2023). Spray-Dried Oregano Oil and Lavender Oil Microcapsules for Antibacterial Sports and Leisurewear. *AATCC Journal of*

*Research*, *10*(6), 332–345. https://doi.org/10.1177/24723444231175211

Vaiani, L., Boccaccio, A., Uva, A. E., Palumbo, G., Piccininni, A., Guglielmi, P., Cantore, S., Santacroce, L., Charitos, I. A., & Ballini, A. (2023). Ceramic materials for biomedical applications: an overview on properties and fabrication processes. *Journal of Functional Biomaterials*, *14*(3), 146.

Vijaya, M. S. (2012). *Piezoelectric materials and devices: applications in engineering and medical sciences*. CRC press.

Vilarinho, P. M. (2005). Functional materials: properties, processing and applications. *Scanning Probe Microscopy: Characterization, Nanofabrication and Device Application of Functional Materials: Proceedings of the NATO Advanced Study Institute on Scanning Probe Microscopy: Characterization, Nanofabrication and Device Application of Functio*, 3–33.

Vouilloz, F. J., Castro, M. S., Vargas, G. E., Gorustovich, A., & Fanovich, M. A. (2017). Reactivity of BaTiO3-Ca10(PO4)6(OH)2 phases in composite materials for biomedical applications. *Ceramics International*, *43*(5), 4212–4221. https://doi.org/10.1016/j.ceramint.2016.12.053

Wang, C., Hu, C., Chen, F., Ma, T., Zhang, Y., & Huang, H. (2023). Design strategies and effect comparisons toward efficient piezocatalytic system. *Nano Energy*, *107*, 108093.

Wang, D., Zhang, Y., & Hong, Z. (2014). Novel fast-setting chitosan/β-dicalcium silicate bone cements with high compressive strength and bioactivity. *Ceramics International*, *40*(7), 9799–9808.

Wang, K., Zhang, M., Li, D., Liu, L., Shao, Z., Li, X., Arandiyan, H., & Liu, S. (2022). Ternary BaCaZrTi perovskite oxide piezocatalysts dancing for efficient hydrogen peroxide generation. *Nano Energy*, *98*, 107251.

Wang, P., Li, Y., & Lu, Y. (2011). Enhanced piezoelectric properties of (Ba0. 85Ca0. 15)(Ti0. 9Zr0. 1) O3 lead-free ceramics by optimizing calcination and sintering temperature. *Journal of the European Ceramic Society*, *31*(11), 2005–2012.

Wang, X., Huan, Y., Zhu, Y., Zhang, P., Yang, W., Li, P., Wei, T., Li, L., & Wang, X. (2022). Defect engineering of BCZT-based piezoelectric ceramics with high piezoelectric properties. *Journal of Advanced Ceramics*, *11*, 184–195.

Wang, Y. (2016). Bioadaptability: an innovative concept for biomaterials. *Journal of Materials Science & Technology*, *32*(9), 801–809.

Wu, F., Wei, J., Guo, H., Chen, F., Hong, H., & Liu, C. (2008). Self-setting bioactive calcium-magnesium phosphate cement with high strength and degradability for bone regeneration. *Acta Biomaterialia*, *4*(6), 1873–1884. https://doi.org/10.1016/j.actbio.2008.06.020

Wu, T., Ji, X., Zhang, Z., Wang, S., Zhou, J., Meng, L., Liu, X., Yu, H., Gong, T., & Liu, Y. (2023). The effects of BaTiO3 on the handleability and mechanical strength of the prepared piezoelectric calcium phosphate silicate for bone tissue engineering. *Ceramics International*, *49*(12), 19746–19752.

Xu, H., Zhuang, Y., Fu, Z., Cui, J., Jiang, S., Zhao, B., & Lin, K. (2024). Promoted osteogenesis by corona discharge poling induced in electroactive piezoelectric bioceramics. *Ceramics International*, *50*(1), 672–683. https://doi.org/10.1016/j.ceramint.2023.10.145

Yan, S., Cao, Z., Liu, Q., Gao, Y., Zhang, H., & Li, G. (2022). Enhanced piezoelectric activity around orthorhombic-tetragonal phase boundary in multielement codoping BaTiO3. *Journal of Alloys and Compounds*, *923*, 166398.

Yu, S.-W., Kuo, S.-T., Tuan, W.-H., Tsai, Y.-Y., & Su, C.-H. (2011). Ion release from three lead-free piezoelectric ceramics and their physical and cytotoxicity characteristics. *Materials Letters*, *65*(23–24), 3522–3524.

Zhang, L., Zhang, M., Wang, L., Zhou, C., Zhang, Z., Yao, Y., Zhang, L., Xue, D., Lou, X., & Ren, X. (2014). Phase transitions and the piezoelectricity around morphotropic phase boundary in Ba(Zr0.2Ti0.8)O3-x(Ba0.7Ca0.3)TiO3 lead-free solid solution. *Applied Physics Letters*, *105*(16), 1–6. https://doi.org/10.1063/1.4899125

Zhang, X., Zhang, C., Lin, Y., Hu, P., Shen, Y., Wang, K., Meng, S., Chai, Y., Dai, X., Liu, X., Liu, Y., Mo, X., Cao, C., Li, S., Deng, X., & Chen, L. (2016). Nanocomposite Membranes Enhance Bone Regeneration Through Restoring Physiological Electric Microenvironment. *ACS Nano*, *10*(8), 7279–7286. https://doi.org/10.1021/acsnano.6b02247

Zhang, Y., Chen, L., Zeng, J., Zhou, K., & Zhang, D. (2014). Aligned porous barium titanate/hydroxyapatite composites with high piezoelectric coefficients for bone tissue engineering. *Materials Science and Engineering C*, *39*(1), 143–149. https://doi.org/10.1016/j.msec.2014.02.022